






Article

Unveiling the Evolutionary State of Three B Supergiant Stars: PU Gem, ϵ CMa, and η CMa

Julieta Paz Sánchez Arias ^{1,*}, Péter Németh ^{1,2}, Elisson Saldanha da Gama de Almeida ³,
Matias Agustin Ruiz Diaz ⁴, Michaela Kraus ¹ and Maximiliano Haucke ⁵

¹ Astronomical Institute, Czech Academy of Sciences, Fričova 298, 25165 Ondřejov, Czech Republic

² Astroserver.org, Főtér 1, 8533 Malomsok, Hungary

³ Instituto de Física y Astronomía, Universidad de Valparaíso, Av. Gran Bretaña 1111, Casilla 5030, Valparaíso, Chile

⁴ Instituto de Astrofísica de La Plata, CONICET-UNLP, Paseo del Bosque s/n, La Plata 1900, Argentina

⁵ Instituto de Ingeniería y Agronomía, Universidad Nacional Arturo Jauretche, Av. Calchaquí 6200, Florencio Varela 1888, Argentina

* Correspondence: julieta.sanchez@asu.cas.cz

Abstract: We aim to combine asteroseismology, spectroscopy, and evolutionary models to establish a comprehensive picture of the evolution of Galactic blue supergiant stars (BSG). To start such an investigation, we selected three BSG candidates for our analysis: HD 42087 (PU Gem), HD 52089 (ϵ CMa), and HD 58350 (η CMa). These stars show pulsations and were suspected to be in an evolutionary stage either preceding or succeeding the red supergiant (RSG) stage. For our analysis, we utilized the 2-min cadence TESS data to study the photometric variability, and we obtained new spectroscopic observations at the CASLEO observatory. We used non-LTE radiative transfer models calculated with CMFGEN to derive their stellar and wind parameters. For the fitting procedure, we included CMFGEN models in the iterative spectral analysis pipeline XTGRID to determine their CNO abundances. The spectral modeling was limited to changing only the effective temperature, surface gravity, CNO abundances, and mass-loss rates. Finally, we compared the derived metal abundances with prediction from Geneva stellar evolution models. The frequency spectra of all three stars show stochastic oscillations and indications of one nonradial strange mode, $f_r = 0.09321 d^{-1}$ in HD 42087 and a rotational splitting centred in $f_2 = 0.36366 d^{-1}$ in HD 52089. We conclude that the rather short sectoral observing windows of TESS prevent establishing a reliable mode identification of low frequencies connected to mass-loss variabilities. The spectral analysis confirmed gradual changes in the mass-loss rates, and the derived CNO abundances comply with the values reported in the literature. We were able to achieve a quantitative match with stellar evolution models for the stellar masses and luminosities. However, the spectroscopic surface abundances turned out to be inconsistent with the theoretical predictions. The stars show N enrichment, typical for CNO cycle processed material, but the abundance ratios did not reflect the associated levels of C and O depletion. We found HD 42087 to be the most consistent with a pre-RSG evolutionary stage, HD 58350 is most likely in a post-RSG evolution and HD 52089 shows stellar parameters compatible with a star at the TAMS.

Keywords: stars: massive; stars: supergiants; stars: winds; outflows



Citation: Sánchez Arias, J.P.; Németh, P.; de Almeida, E.S.G.; Ruiz Diaz, M.A.; Kraus, M.; Haucke, M. Unveiling the Evolutionary State of Three B Supergiant Stars: PU Gem, ϵ CMa, and η CMa. *Galaxies* **2023**, *11*, 93. <https://doi.org/10.3390/galaxies11050093>

Academic Editor: Jorick Sandor Vink

Received: 17 March 2023

Revised: 19 August 2023

Accepted: 23 August 2023

Published: 29 August 2023



Copyright: © 2023 by the authors. Licensee MDPI, Basel, Switzerland. This article is an open access article distributed under the terms and conditions of the Creative Commons Attribution (CC BY) license (<https://creativecommons.org/licenses/by/4.0/>).

1. Introduction

Massive stars are one of the most important objects in the universe due to their key role in the enrichment of interstellar medium with metals for future star generations, as well as in the evolution of host galaxies [1]. Nevertheless, understanding their evolution is challenging due to the significant changes they experience at different evolutionary stages, especially during the post-Main Sequence (MS). Therefore, any inaccuracy in the input

parameters results in large uncertainties of the evolutionary models [2,3]. Fortunately, there are many sophisticated stellar evolutionary models calculated for massive stars e.g., [4,5]. However, they depend on internal parameters such as rotation, chemical mixing, and angular momentum transport, for which no decisive observational constraints are available. In addition, massive supergiant stars undergo mass loss via line-driven winds, and their rates are far from being firmly established, adding even more uncertainties to the evolution of these stars.

BSGs comprise extreme transition phases, in which the stars shed huge amounts of material into their environments. During the evolution of massive stars, those stars with masses between 20 and 40 M_{\odot} evolve back to the blue supergiant state after a Red Supergiant (RSG) state, either as a Blue Supergiant (BSG) or in a follow-up Wolf-Rayet phase. On the other hand, massive stars with $<20 M_{\odot}$ may experience “blue loops”, where the star changes from a cool star to a hotter one before cooling again. Therefore, hot BSGs can be found at the pre-RSG stage, burning only H in a shell or at the post-RSG during the He-core burning. The exact reason why some massive stars experience “blue loops” and others do not still remains unknown, although it is known that extra mixing processes within the layers surrounding their convective core, along with mass-loss events during their evolution, play an essential role [6–8].

In addition, BSGs can show an extremely rich spectrum of stellar oscillations. Since these oscillations depend on the internal structure of the star, their analysis paves the way to understanding phenomena such as the occurrence of “blue loops” or the discernment between the different evolutionary stages in which blue supergiant stars can exist. The observed oscillation modes in B supergiants are driven by different excitation mechanisms, such as the classical κ mechanism, stochastic wave generation caused by the presence of convective layers in the outer regions of the star or in their envelope, and tidal excitation causing the so-called Rossby modes and strange modes. Strange modes are nonlinear instabilities that require a luminosity over a mass ratio of $L_{\star}/M_{\star} > 10^4 L_{\odot}/M_{\odot}$ to be excited [9]. Their existence has been related to the variable mass loss these stars experience [10–12].

Recent studies on stellar oscillations of individual BSGs [10,12,13] improved our understanding of the complex variability shown by these stars. Furthermore, considerable progress has been made in theoretical studies on the stellar oscillations of massive stars at different evolutionary stages focusing on specific mass ranges. For example, ref. [14] investigated stellar oscillations in stars at pre- and post-RSG stages for masses between 13 and 18 solar masses for different physical parameters such as metallicity and overshooting. In [15], a thorough study of stellar oscillations is presented for a broader range of masses, revealing that the pulsation properties in pre- and post-RSG evolutionary phases are fundamentally different: stars in the post-RSG stage pulsate in many more modes, including radial strange modes, than their less evolved counterparts, although these authors did not inspect the effect of different wind efficiency on the stability of the modes.

Despite the efforts accumulated over years in the study of the stellar pulsations of these objects in different evolutionary stages, the correct identification of the evolutionary stage of BSGs additionally requires a detailed analysis of spectral observations due to the large uncertainties these stars have in astrophysics parameters such as the mass and the radii.

Therefore, we started a comprehensive study of these objects with the aim of gaining insights into the evolutionary state of BSG stars. Combining information about the pulsation behavior extracted from photometric lightcurves with newly determined stellar parameters and precise chemical abundances obtained from the modeling of acquired spectroscopic data, we strive to find clear evidence for either a pre- or a post-RSG state of the objects. The current paper presents our methodology and first results on a small sample of objects.

This paper is organized as follows: in Section 2, we summarize the main parameters for these stars found in the literature; Section 3 describes the spectroscopic and photometric observations employed in this work. In Section 4, we present the analysis of the light curves and the frequency spectra. Section 5 is devoted to the spectral analysis of the selected objects.

We describe the numerical tools employed, including brand new capabilities implemented in XTGRID [16] for this work and the results obtained. Finally, Sections 6 and 7 are devoted to the discussion and conclusions.

2. Target Selection and Parameters Values from Literature

Haucke et al. [11] presented the most recent comprehensive analysis of the wind properties of 19 pulsating BSGs. We focus on three objects from their sample, for which we have obtained new spectroscopic observations. These are the stars HD 42087 (PU Gem), HD 52089 (ϵ CMA), and HD 58350 (η CMA). Table 1 summarizes the values for these stars derived by Haucke et al. [11]. They serve as reference (or starting) values for our analysis. In Figure 1, we show the position of the selected stars in an HR diagram for the parameters in Table 1. We notice that these hot BSG stars could be either at the immediate post-Main Sequence or at the post-Red Supergiant stage.

The three selected objects have been studied extensively in the literature, and a compilation of literature values for their stellar and wind parameters can be found in Haucke et al. [11]. Here, we present a brief overview highlighting a variety of stellar and wind parameters.

2.1. HD 42087

Searle et al. [17] derived the following parameters for this star using spectra from October 1990: $T_{\text{eff}} = 18,000 \pm 1000$ K, $\log g = 2.5$, $\log(L_*/L_\odot) = 5.11 \pm 0.24$, $R_* = 36.6 R_\odot$, and $v \sin i = 71$ km s⁻¹. They employed CMFGEN complemented with TLUSTY to derive T_{eff} and $\log(L_*/L_\odot)$, $\log g$, along with the CNO abundances, which were $\epsilon(\text{C}) = 7.76$, $\epsilon(\text{N}) = 8.11$, and $\epsilon(\text{O}) = 8.80$. For the wind parameters, they obtained $\dot{M} = 5.0 \times 10^{-7} M_\odot \text{ yr}^{-1}$, $\beta = 1.2$, and $v_\infty = 650$ km s⁻¹. Morel et al. [18] showed that HD 42087 has a high H α variability with a spectral variability index (as defined by these authors) of $\sim 91\%$ in this line (see Section 4 of [18]), evidencing a cyclic behaviour with P ~ 25 d. We also mention that the values derived for this object in Haucke et al. [11] were obtained with TLUSTY using an optical spectrum covering only the H α region. These spectra from 2006 showed a P Cygni feature with a weak emission and a strong absorption component.

2.2. HD 52089

In Morel et al. [19], this star was studied as a slowly rotating B-type dwarf star. They derived $T_{\text{eff}} = 23,000$ K and $\log g = 3.30 \pm 0.15$ using spectroscopic data from April 2005. By using the DETAIL/SURFACE code, they determined the non-LTE abundances $\epsilon(\text{C}) = 8.09 \pm 0.12$, $\epsilon(\text{N}) = 7.93 \pm 0.24$, and $\epsilon(\text{O}) = 8.44 \pm 0.18$. Fossati et al. [20] derived an effective temperature and surface gravity of $T_{\text{eff}} = 22\,500 \pm 300$ K and $\log g = 3.40 \pm 0.08$. They also obtained updated values for the surface abundances by analyzing a FEROS spectra from 2011 and found $\epsilon(\text{C}) = 8.30 \pm 0.07$, $\epsilon(\text{N}) = 8.16 \pm 0.07$ and $\epsilon(\text{O}) = 8.70 \pm 0.12$. Additionally, they estimated a $12.5 M_\odot$ for this object.

2.3. HD 58350

Lefever et al. [21] derived $T_{\text{eff}} = 13,500$ K, $\log g = 1.75$, $R_* = 65 R_\odot$, $\log(L_*/L_\odot) = 5.10$, $v_\infty = 250$ km s⁻¹, $\dot{M} = 1.4 \times 10^{-7} M_\odot \text{ yr}^{-1}$ and $\beta = 2.5$ for the stellar and wind parameters of this star. In Searle et al. [17], they derived $T_{\text{eff}} = 15,000 \pm 500$ K, $\log g = 2.13$, $R_* = 57.3 \pm 2.64 R_\odot$, and $\log(L_*/L_\odot) = 5.18 \pm 0.17$. For the CNO abundances, they obtained $\epsilon(\text{C}) = 7.78$, $\epsilon(\text{N}) = 8.29$, and $\epsilon(\text{O}) = 8.75$.

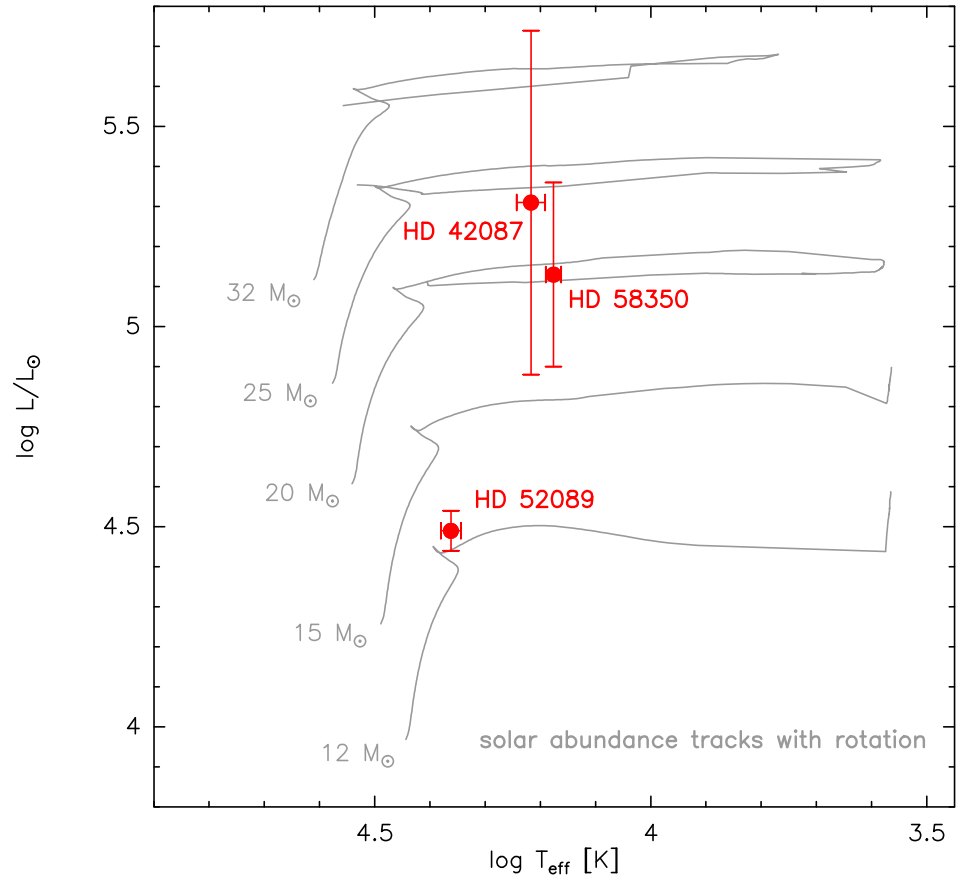


Figure 1. Our three BSG stars in the HR diagram according to the values derived in [11]. The evolutionary tracks are taken from [22].

Table 1. Stellar and wind parameters derived by Haucke et al. [11] for our star sample.

Parameter	HD 42087	HD 52089	HD 58350
$T_{\text{eff}} [\text{K}]$	$16,500 \pm 1000$	$23,000 \pm 1000$	$15,500 \pm 700$
$\log g [\text{cgs}]$	2.45 ± 0.10	3.00 ± 0.10	2.00 ± 0.10
$\log L_{\star} [L_{\odot}]$	5.31 ± 0.43	4.49 ± 0.05	5.18 ± 0.32
$R_{\star} [R_{\odot}]$	55	11	54
$v \sin i [\text{km s}^{-1}]$	80	10	40
$\dot{M} [M_{\odot} \text{ yr}^{-1}]$	$(5.7 \pm 0.5) \times 10^{-7}$	$(2.0 \pm 0.6) \times 10^{-8}$	$(1.4 \pm 0.2) \times 10^{-7}$
$v_{\infty} [\text{km s}^{-1}]$	700 ± 70	900 ± 270	200 ± 30
β	2.0	1.0	3.0

3. Observations

With the aim of shedding light on the evolutionary state of these objects, we analyze new spectroscopic observations and combine these results with information extracted from their photometric light curves.

3.1. Spectra

The spectra we employed in this work to derive new parameters were taken on 23 and 24 January 2020 for HD 42087 and HD 58350, respectively, and 14 February 2015 for HD 52089. All of them cover the wavelength range from 4275 Å up to 6800 Å with a signal-to-noise ratio S/N of 140, 140, and 130 for HD 42087, HD 52089, and HD 58350, respectively.

We utilized the REOSC spectrograph attached to the Jorge Sahade 2.15 m telescope at the Complejo Astronómico El Leoncito (CASLEO), San Juan, Argentina. The resolving

power at 4500 Å and 6500 Å is $R \sim 12,600$ and $R \sim 13,900$, respectively. The spectra were reduced and normalized following standard procedures using IRAF¹ routines.

In order to show the H α variability in our targets, we have collected previous observations in CASLEO, depicted in Figures 2–4; from 15 January 2006 for HD 42087; 5 February 2013 for HD 52089; and 15 January 2006 and 5 February 2013 for HD 58350.

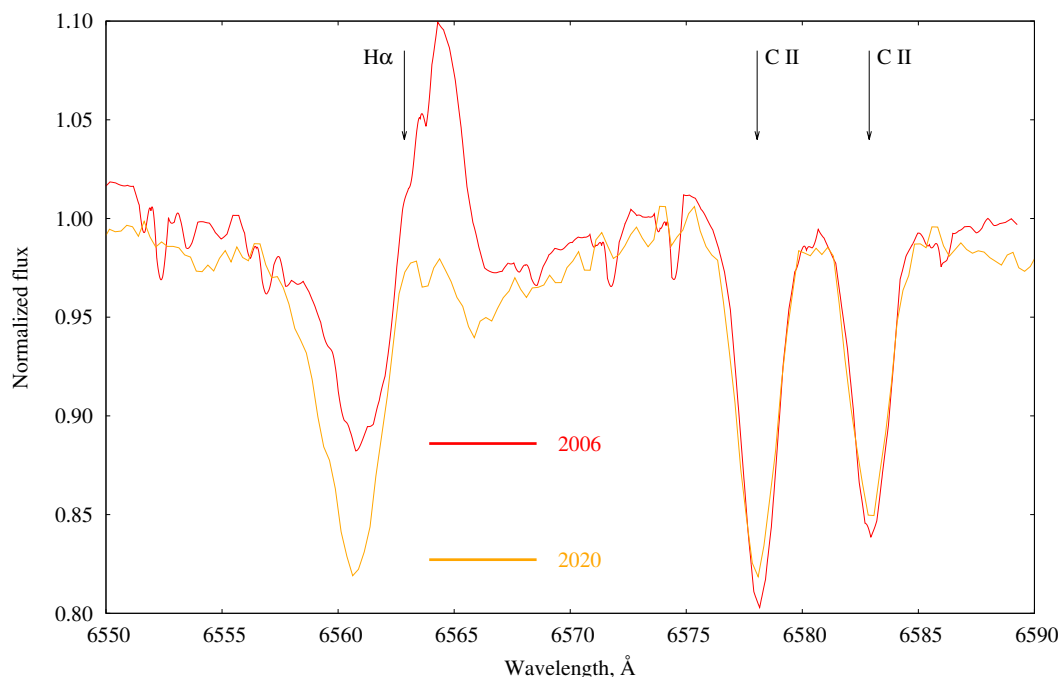


Figure 2. Evolution of the H α line profile of HD 42087 between 2006 and 2020. The emission component weakened by 2020.

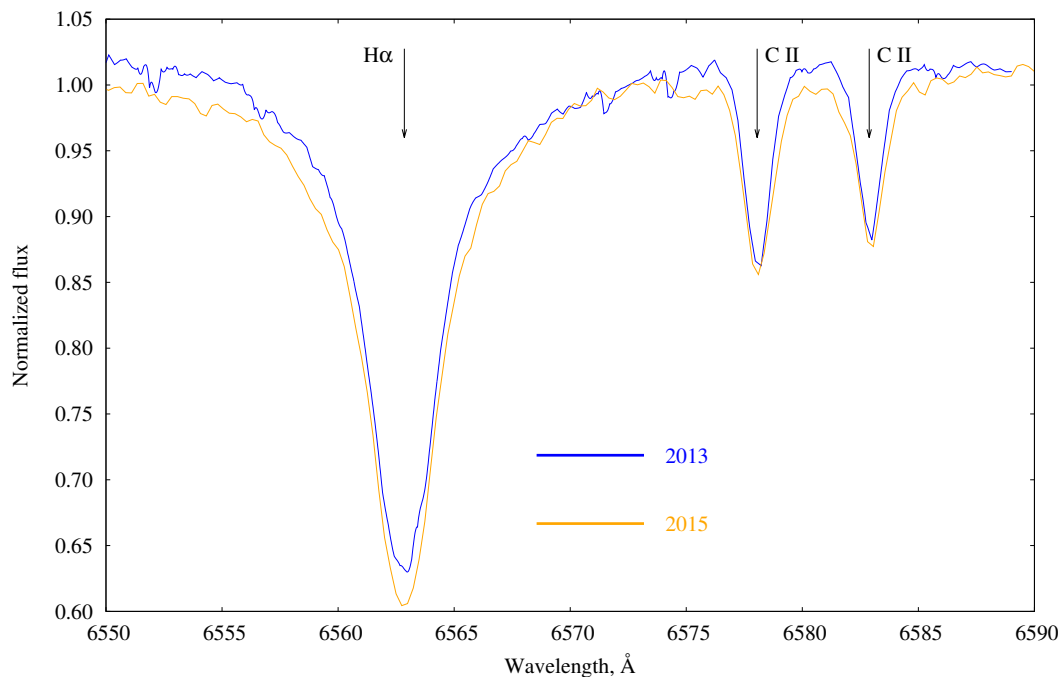


Figure 3. Evolution of the H α line profile of HD 52089 between 2013 and 2015.

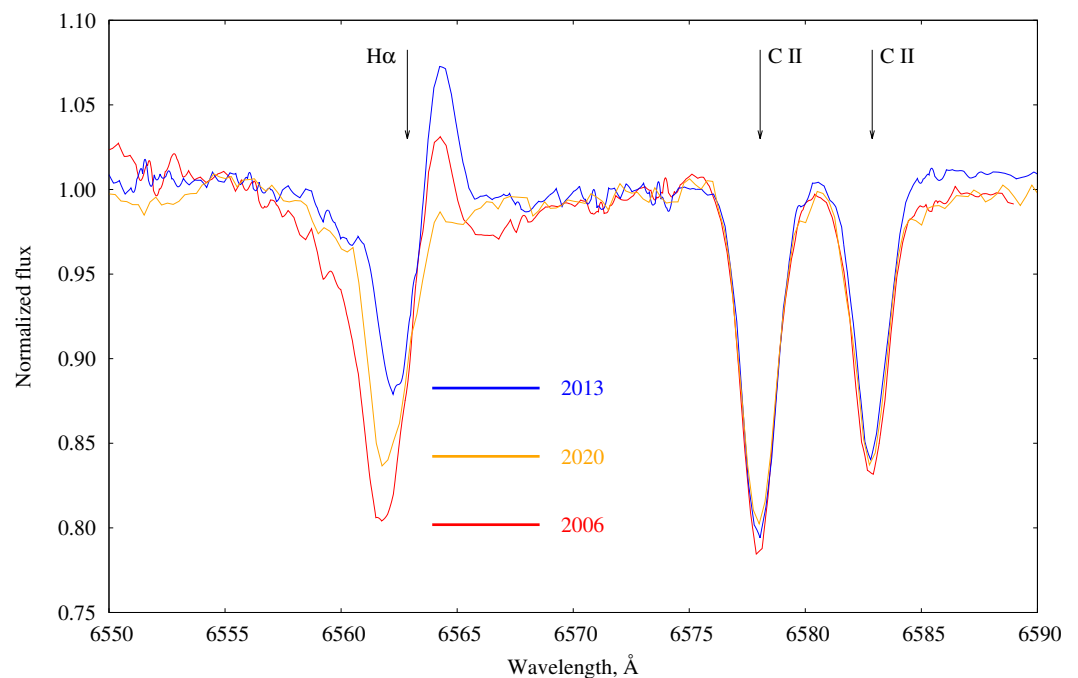


Figure 4. Evolution of the H α line profile of HD 58350 between 2006 and 2020. The emission component has strengthened between 2006 and 2013 and became noticeably weaker by 2020.

3.2. Photometric Light Curves

We complemented the optical spectra with space photometry collected with the Transiting Exoplanet Survey Satellite (TESS) mission [23,24]. We retrieved a high cadence (120 s) PDCSAP light curve for each object using Astroquery [25] and cleaned the light curves using the Lightkurve package [26]. For this, we first selected only the data points with a quality flag equal to 0, meaning they are not cosmic rays or data from bad pixels. Next, we carried out sigma clipping to remove outliers, using a value of 6σ for all light curves, following a similar procedure as in Garcia et al. [27]. The resulting light curves were transformed to display the variation of the magnitude (Δm) from the mean magnitude:

$$\Delta m = -2.5 \log(\text{pdcsap_flux}) + 2.5 \log(\overline{\text{pdcsap_flux}}); \quad (1)$$

where pdcsap_flux is the individual flux at each exposure and $\overline{\text{pdcsap_flux}}$ is the mean flux of the entire light curve. In this way, we obtain a normalized light curve, whose amplitude can be expressed in units of mag. The time axis is in units of Barycentric Julian Date, which is the Julian Date corrected for differences in the earth's position with respect to the barycenter of the solar system.

4. Frequency Analysis

We employed the Fourier Transform with Period04 [28]. For each star and sector, the frequencies were searched in the interval $[0;50] d^{-1}$, widely covering their frequency content. No frequency beyond $2 d^{-1}$ was found for any star. The amplitude and phase were calculated using a least square sine fit for each detected frequency. After obtaining the first frequency, the analysis was performed on the residuals. The Fourier analysis was stopped after obtaining 15 frequencies. Once we derived the frequencies following this procedure, we dismissed those frequencies below $0.1 d^{-1}$ since TESS data of a single sector do not allow us to derive periods higher than ~ 10 d. Additionally, we discard those frequencies with a separation of less than $2/T$, where $1/T$ is the Rayleigh resolution and T is the time span of the observations. The S/N ratio was computed for the derived frequencies along with the uncoupled uncertainties in the frequencies and amplitudes using a Monte Carlo simulation.

When available, we also analyzed the frequency content of the combined, consecutive sectors, since the longer time baseline would facilitate the detection of longer periods from radial modes possibly connected to strange modes. We considered the values recommended in Baran and Koen [29] for the S/N when dealing with individual TESS sectors and combined sectors, which resulted in 5.037 for our individual TESS sectors, and of 5.124 and 5.194 for the combined sectors of HD 52089 (2 sectors combined) and HD 42087 (3 sectors combined), respectively. Nevertheless, we took into account frequencies with lower S/N whenever they turned out to be interesting for the analysis (see below).

Finally, when comparing frequencies from different sectors, we adopted the separation criterion for the combined sectors.

Next, we provide the details of the light curves and the frequencies extracted for each star.

4.1. HD 42087

This star was observed in 3 consecutive sectors: Sector 43, in the period from 16 September to 10 October 2021; Sector 44, from 10 October to 6 November 2021; and Sector 45, from 6 November to 2 December 2021, covering an observation time span of 24.287 days, 24.156 days and 24.551 days, respectively. The light curve and the amplitude spectra for the individual sectors and all sectors combined are displayed in Figure 5.

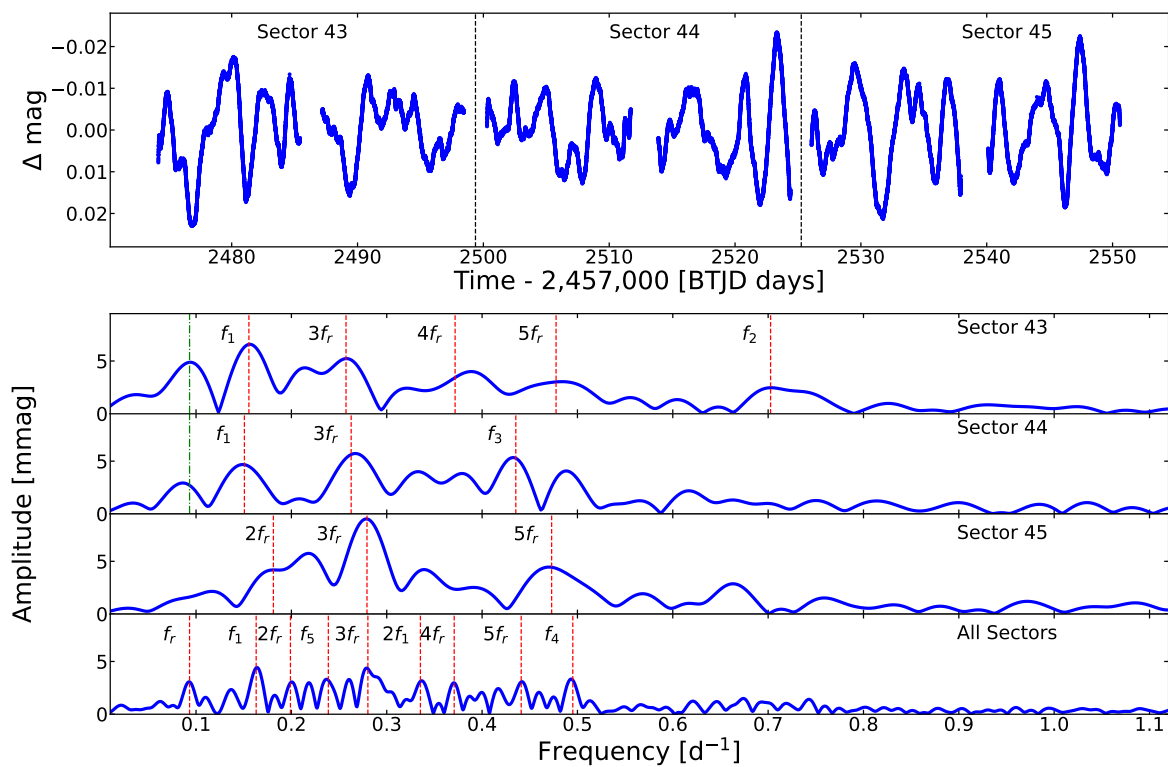


Figure 5. Top panel: Light curve of HD 42087 corresponding to Sectors 43, 44, and 45. Lower panels: Amplitude spectra for each sector and all sectors combined.

The frequencies derived for sectors 43, 44, and 45 are listed in Table 2 and the threshold considered for the frequency separation is $0.0823 d^{-1}$, $0.0828 d^{-1}$ and $0.0815 d^{-1}$, respectively. For the analysis of all sectors combined, the time span is $T = 72.994 d$; therefore, the separation criterion we employed is $2/T = 0.0274 d^{-1}$. We adopted this value as a conservative threshold when comparing frequencies from different sectors.

Table 2. List of frequencies, their amplitudes, and S/N ratios, found for HD 42087.

Sector	Frequency [d^{-1}]	$3\sigma_f$ [d^{-1}]	Amplitude [mmag]	$3\sigma_A$ [mmag]	S/N	Id
43	0.15543	0.00044	7.7615	0.15	10.65	f_1
	0.25729	0.00063	5.7467	0.14	8.41	$3 \times f_r$
	0.47759	0.00064	4.7663	0.13	7.79	$5 \times f_r$
	0.37169	0.00090	3.5347	0.13	5.45	$4 \times f_r$
	0.70257	0.00037	2.9734	0.14	5.41	f_2
44	0.26268	0.00068	5.5317	0.16	7.68	$3 \times f_r$
	0.15072	0.00082	5.2203	0.17	6.75	f_1
	0.43536	0.00090	4.9832	0.19	7.45	f_3
45	0.27928	0.00009	9.2074	0.10	10.65	$3 \times f_r$
	0.18110	0.00059	5.0188	0.13	5.57	$2 \times f_r$
	0.47295	0.00159	4.0068	0.21	5.07	$5 \times f_r$
All	0.28022	0.00019	4.4715	0.12	8.48	$3 \times f_r$
	0.16305	0.00021	3.9728	0.11	7.05	f_1
	0.49515	0.00022	3.4982	0.11	7.44	f_4
	0.23874	0.00027	3.2680	0.11	6.04	f_5
	0.44102	0.00023	3.2321	0.10	6.67	$5 \times f_r$
	0.33531	0.00030	2.9450	0.11	5.74	$2 \times f_1$
	0.19899	0.00029	2.8086	0.10	5.07	$2 \times f_r$
	0.37073	0.00033	2.6635	0.10	5.29	$4 \times f_r$
	0.09321	0.00032	2.4597	0.12	4.20	f_r

The pulsational content of HD 42087 lies at low frequencies below $0.8 d^{-1}$ and the amplitudes are between 2.5 and 9.5 mmag, approximately. When analyzing the combined sectors, we also searched for frequencies down to $0.025 d^{-1}$ due to the extended length of the observations. This allowed us to find the frequency f_r and its five harmonics. Some of these harmonics appear in the individual sectors. Due to the short time span for individual sectors, frequencies below $\sim 0.1 d^{-1}$ are not reliable; nevertheless, f_r seems to appear for sectors 43 and 44 (indicated with green lines in Figure 5). Besides f_r and its harmonics, five frequencies appear randomly over the four sets of observations, which are likely related to stochastic oscillations (see Section 6).

4.2. HD 52089

This star was observed in 4 TESS sectors: Sector 6, in the period from 15 December 2018 to 6 January 2019; Sector 7, in the period from 8 January to 1 February 2019; Sector 33 from 18 December 2020 to 13 January 2021; and Sector 34 in the period from 13 January to 8 February 2021. The total time spans for Sectors 6, 7, 33, and 34 are 21.771 d, 24.454 d, 25.839 d, and 24.962 d, respectively. Figure 6 displays the light curves and amplitude spectra for Sectors 6 and 7, and Figure 7 displays the same information for Sectors 33 and 34. Due to the large time gap between sectors 7 and 33, we decided to evaluate the sectors in pairs; i.e., together with the analysis of sectors 6 and 7, we studied the frequencies of these sectors combined, and the same with sectors 33 and 34. For the combined sectors 6 and 7, the time span is 46.225 d, and for sectors 33 and 34 together, the time span is 50.801 d.

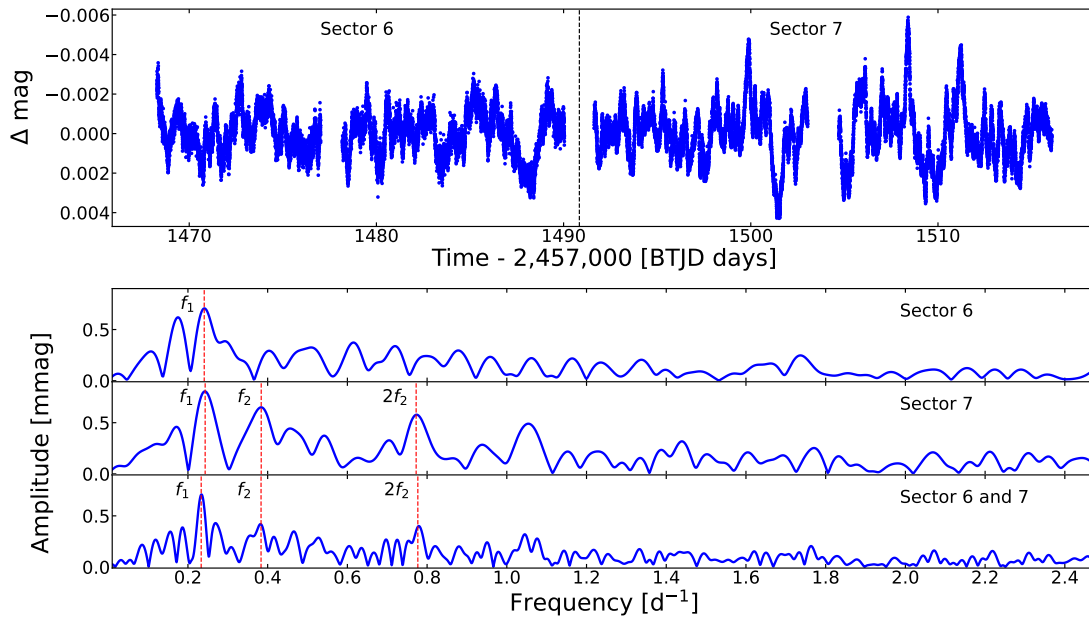


Figure 6. Top panel: Light curve of HD 52089 corresponding to Sectors 6 and 7. Lower panels: Amplitude spectra for each sector and all sectors combined.

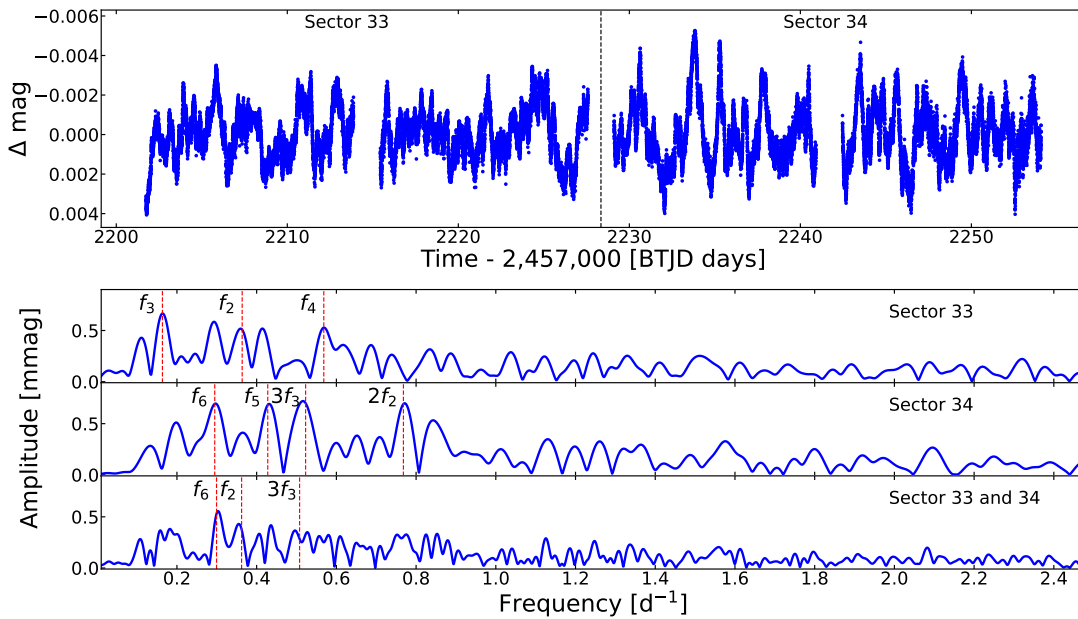


Figure 7. Top panel: Light curve of HD 52089 corresponding to Sectors 33 and 34. Lower panels: Amplitude spectra for each sector and all sectors combined.

The derived frequencies, their amplitudes and identifications are listed in Table 3. The separation criteria we employed are $0.0918 d^{-1}$, $0.0817 d^{-1}$, $0.0774 d^{-1}$, and $0.0801 d^{-1}$ for sectors 6, 7, 33, and 34, respectively. For sectors 6 and 7 combined and 33 and 34 combined the separation criteria are $0.0432 d^{-1}$ and $0.0393 d^{-1}$, respectively and the lowest detectable frequency for the sectors combined is $\sim 0.04 d^{-1}$. We adopted conservative separation criteria with $0.0393 d^{-1}$ to compare frequencies from different sectors. We find only one significant frequency, f_1 , in Sector 6, which is also in Sector 7. In Sector 7, we found another frequency, f_2 , which stays present also in Sector 33, and its harmonic, which appears in Sector 34. We searched for lower frequencies in both combined light curves, but we did not find any. After the gap of ~ 2 years in the observations, new frequencies appear randomly

in the new Sectors, which indicates they are not related to stellar oscillations due to their short lifetime (f_3, f_5, f_6). We note that $f_2 - f_3 \sim f_4 - f_2$ in Sector 33, indicating the presence of a triplet centred in f_2 with a possible rotation frequency of $0.20 d^{-1}$. Nevertheless, the observations' short time span makes precise classification difficult. We did not find any significant frequency at lower ranges in the combined sectors.

Table 3. Sector, Frequency, Amplitude, and Identification for HD 52089.

Sector	Frequency [d^{-1}]	$3\sigma_f$ [d^{-1}]	Amplitude [mmag]	$3\sigma_A$ [mmag]	S/N	Id
6	0.24083	0.00115	0.7830	0.05	6.15	f_1
7	0.24316	0.01540	0.8982	0.47	6.14	f_1
	0.38381	0.00192	0.7286	0.05	5.15	f_2
	0.77252	0.00051	0.5888	0.02	4.37	$2 \times f_2$
6 & 7	0.23321	0.00072	0.7736	0.07	7.28	f_1
	0.38342	0.02775	0.4930	0.17	4.79	f_2
	0.77679	0.00073	0.4769	0.04	4.83	$2 \times f_2$
33	0.16358	0.00070	0.7716	0.02	6.868	f_3
	0.36366	0.00089	0.5784	0.02	5.42	f_2
	0.56843	0.00089	0.5083	0.02	4.72	f_4
34	0.42781	0.00107	0.7556	0.03	4.98	f_5
	0.52280	0.00128	0.7113	0.03	4.74	$3 \times f_3$
	0.76818	0.00127	0.7038	0.03	4.75	$2 \times f_2$
	0.29483	0.00147	0.6389	0.03	4.35	f_6
33 & 34	0.29937	0.00167	0.6627	0.12	5.01	f_6
	0.36220	0.00331	0.5806	0.34	4.39	f_2
	0.50772	0.00158	0.4714	0.09	4.09	$3 \times f_3$

4.3. HD 58350

This star has been observed in Sector 34 in the period from 14 January to 8 February 2021, covering a total timespan of $T = 24.96$ days. The light curve for Sector 34 is displayed in the top panel of Figure 8, and we show the amplitude spectra in the lower panel.

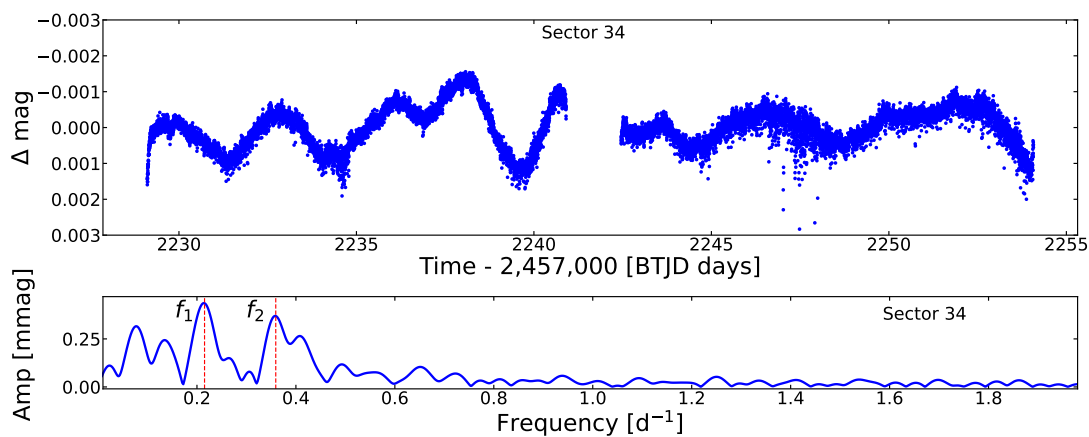


Figure 8. Top panel: Light curve of HD 58350 acquired during Sector 34. Lower panel: Amplitude spectrum for the same sector.

The resulting list of frequencies for HD 58350 is shown in Table 4. The separation criterion is $2/T = 0.0801 d^{-1}$. The pulsational content for this BSG lies below $0.5 d^{-1}$. We found two independent frequencies with similar amplitudes.

Table 4. Sector, Frequency, Amplitude, and Identification for HD 58350.

Sector	Frequency [d^{-1}]	$3\sigma_f$ [d^{-1}]	Amplitude [mmag]	$3\sigma_A$ [mmag]	S/N	Id
34	0.21533	0.00069	0.4392	0.01	8.54	f_1
	0.35927	0.00088	0.3339	0.01	7.07	f_2

5. Modeling Tools for Spectral Analysis

5.1. The Code CMFGEN

CMFGEN [30] is one of the state-of-the-art 1-D non-LTE radiative transfer codes for studying the physical and chemical properties of massive hot stars. It has been successfully used for reproducing different types of observables of massive stars, such as in the case of OB supergiants: photometry, spectroscopy, and interferometry, e.g., [17,31,32].

CMFGEN solves the radiative transfer and statistical equilibrium equations for the photosphere and wind under the assumption of radiative equilibrium and considers a spherically symmetric stationary wind. For the photospheric region, CMFGEN solves the radiative transfer and hydrostatic equations (describing the state of radiation and gas in the photosphere) in a self-consistent way. Further details on this procedure can be found in Section 3.1 of Bouret et al. [33].

The wind velocity, $v(r)$, and density, $\rho(r)$, profiles are related to each other as follows, based on the assumption of a stationary and spherical symmetric wind:

$$\dot{M} = 4\pi r^2 \rho(r) v(r) f(r), \quad (2)$$

where r is the distance from the center of the star and \dot{M} is the wind mass-loss rate, which is constant at any location of the wind. Here, the volume filling factor $f(r)$ parameterizes the inclusion of micro-clumping; e.g., [34], that is, inhomogeneities that are found in the winds of massive stars, e.g., [35,36]. In CMFGEN, this parameterization is performed as follows:

$$f(r) = f_\infty + (1 - f_\infty) e^{-\frac{v(r)}{v_{\text{initial}}}}, \quad (3)$$

where f_∞ is the filling factor value at $r \rightarrow \infty$, and v_{initial} is the onset velocity of clumping in the wind. Since our initial guesses in the fitting procedure (as described in Section 5.2) for the stellar and wind parameters are based on the results from Haucke et al. [11], we set $f_\infty = 1.0$ in our default models. This means that our default CMFGEN models are calculated considering a homogeneous wind.

Furthermore, the wind's velocity profile is parameterized in CMFGEN by the so-called β -law approximation, as follows:

$$v(r) = v_\infty \left(1 - \frac{R_\star}{r}\right)^\beta, \quad (4)$$

where v_∞ is the wind terminal velocity and R_\star is the stellar radius (r higher than R_\star). For OB supergiants, values of β are usually found to be as high as ~ 2.0 – 3.0 , e.g., [37]. In short, Equations (2) and (4) sets the relation between the most important and fundamental physical wind parameters: the wind mass-loss rate and the terminal velocity.

Despite its high computational cost, when compared to other non-LTE codes, such as FASTWIND, one of the biggest advantages of CMFGEN relies on its allowance to set a complex chemical composition, with the inclusion of energy levels of different ions from hydrogen up to nickel. For instance, Haucke et al. [11] studied our star sample of three BSGs employing radiative transfer models calculated with FASTWIND considering hydrogen, helium, and silicon with an approximation for the treatment of the line transfer of iron-group elements. In fact, the main difference between these two codes relies on an “exact” treatment of line-blanketing that is performed by CMFGEN (e.g., see [38] and references therein). Table 5 summarizes the atomic species, the number of energy levels, and bound–bound transitions that are included as the default in our models. Our models are calculated considering a robust atomic model for studying massive hot stars, including species of hydrogen, helium, carbon, nitrogen, oxygen, neon, magnesium, silicon, sulfur, iron, and nickel.

Finally, due to the complexity of the code and its computational cost, a very common approach when using CMFGEN is to vary its parameters manually in order to find an acceptable “by eye” fit to the observations, e.g., [32,39–42]. However, in this paper, we implement an automatic fitting procedure with CMFGEN to find the best-fit models for the observed spectrum of each star, as described below.

5.2. Spectral Analysis with XTgrid

XTGRID [16] is a steepest-descent iterative χ^2 minimizing fit procedure to model hot star spectra. The procedure was developed for the model atmosphere code TLUSTY [43–45] and was previously applied to ultraviolet and optical spectral observations of O and B-type stars [10], Horizontal Branch stars [46], hot subdwarfs [47–49], and white dwarfs [50,51]. It was designed to perform fully automated or supervised spectral analyses of massive data sets. The procedure starts with an input model; by applying successive approximations along a decreasing global χ^2 , it iteratively converges on the best solution. All models are calculated on the fly, which is the main advantage of the procedure. XTGRID does not require a precalculated grid; with its tailor-made models—although at a high computational cost—it is able to address nonlinearities in a multidimensional parameter space. After the fitting procedure has converged for a relative change less than 0.5%, parameter errors are evaluated in one dimension, changing each parameter until the χ^2 variation corresponds to the 60% confidence limit. Parameter correlations are evaluated only for the effective temperature and surface gravity. If the procedure finds a better solution during error calculations, it returns to the descent part using the previous solution as the initial model.

Instead of using TLUSTY (plane-parallel model, no wind), we used CMFGEN, since these stars have non-negligible stellar winds with mass-loss rates in the order of 10^{-8} – $10^{-7} M_{\odot} \text{ yr}^{-1}$. Using TLUSTY, instead of CMFGEN, would prevent us to address the wind variability and perform homogeneous modeling for BSGs. In addition, beyond the short-term photometric variability that is typical for pulsating stars and discussed in Section 4, gradual spectral variations may occur due to inhomogeneities in the wind density structure. These, together, require re-evaluating the surface and wind parameters for each observation. Therefore, we decided to proceed with CMFGEN models and start out from the results of Haucke et al. [11]. We updated XTGRID to apply CMFGEN and minimize the wind properties along with stellar surface parameters. Then, we performed a new analysis of the most recent CASLEO spectra to measure the CNO abundances in each of the three stars.

The focus of our analysis was on the CNO abundances. Therefore, we kept the abundances of all elements heavier than O at their solar values [52], and we adopted He abundances $n\text{He}/n\text{H} = 0.2$, based on the analysis of Searle et al. [17]. To maintain an approximate consistency with the results of Haucke et al. [11], we kept the stellar radii and turbulent velocity fixed at the values determined in the previous analysis (see Table 1), and we applied unclumped wind models. Adopting clumping in our models resulted in different mass-loss rates. We neglected macroturbulence in the current analysis because it shows a degeneracy with the projected rotation at low spectral resolutions. We note that

our goal was to measure the CNO abundances and not to make a comparison with the analysis of Haucke et al. [11]. Our method is not suitable for such a comparison; as we used different model atmosphere codes, our observations were taken at different epochs and we used a different fitting procedure.

Table 5. Summary on the atoms and ionization states of our default CMFGEN models, including number of energy levels, super-levels, and bound–bound transitions for each atomic species.

Ion	Full-Levels	Super-Levels	b-b Transitions
H I	30	30	435
He I	69	69	905
He II	30	30	435
C II	322	92	7742
C III	243	99	5528
C IV	64	64	1446
N II	105	59	898
N III	287	57	6223
N IV	70	44	440
N V	49	41	519
O II	274	155	5880
O III	104	36	761
O IV	64	30	359
O V	56	32	314
Ne II	48	14	328
Ne III	71	23	460
Ne IV	52	17	315
Mg II	44	36	348
Si II	53	27	278
Si III	90	51	640
Si IV	66	66	1090
S III	78	39	520
S IV	108	40	958
S V	144	37	1673
Fe II	295	24	2135
Fe III	607	65	6670
Fe IV	1000	100	37,899
Fe V	1000	139	37,737
Fe VI	1000	59	36,431
Ni II	158	27	1668
Ni III	150	24	1345
Ni IV	200	36	2337
Ni V	183	46	1524
Ni VI	182	40	1895

Finally, our best-fit CMFGEN models to the CASLEO spectra of HD 42087, HD 52089, and HD 58350, are shown, respectively, in Figures 9–11, and the derived parameters are listed in Table 6. The luminosity and mass in this table were derived using $L_{\star} = 4\pi R_{\star}^2 \sigma T_{\text{eff}}^4$ and $g = GM_{\star}/R_{\star}^2$.

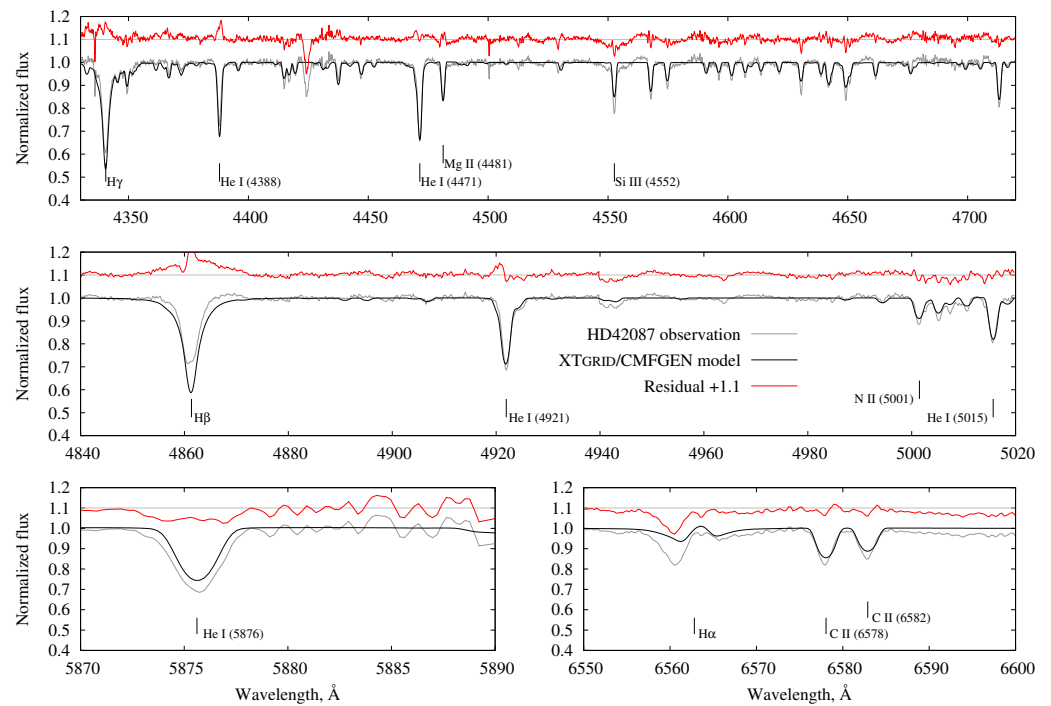


Figure 9. Best-fit XTGRID/CMFGEN model for HD 42087. In each panel, the CASLEO observation is in grey, the CMFGEN model in black, and the residuals, shifted by +1.1 for clarity, are in red.

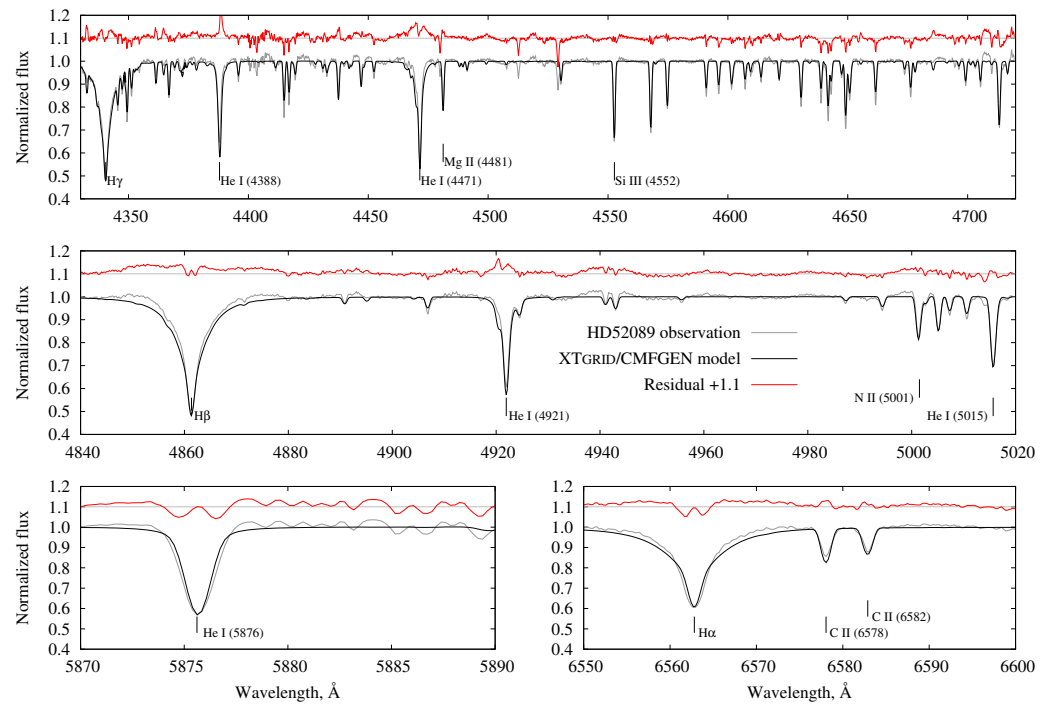


Figure 10. Best-fit XTGRID/CMFGEN model for HD 52089. In each panel, the CASLEO observation is in grey, the CMFGEN model in black, and the residuals, shifted by +1.1 for clarity, are in red.

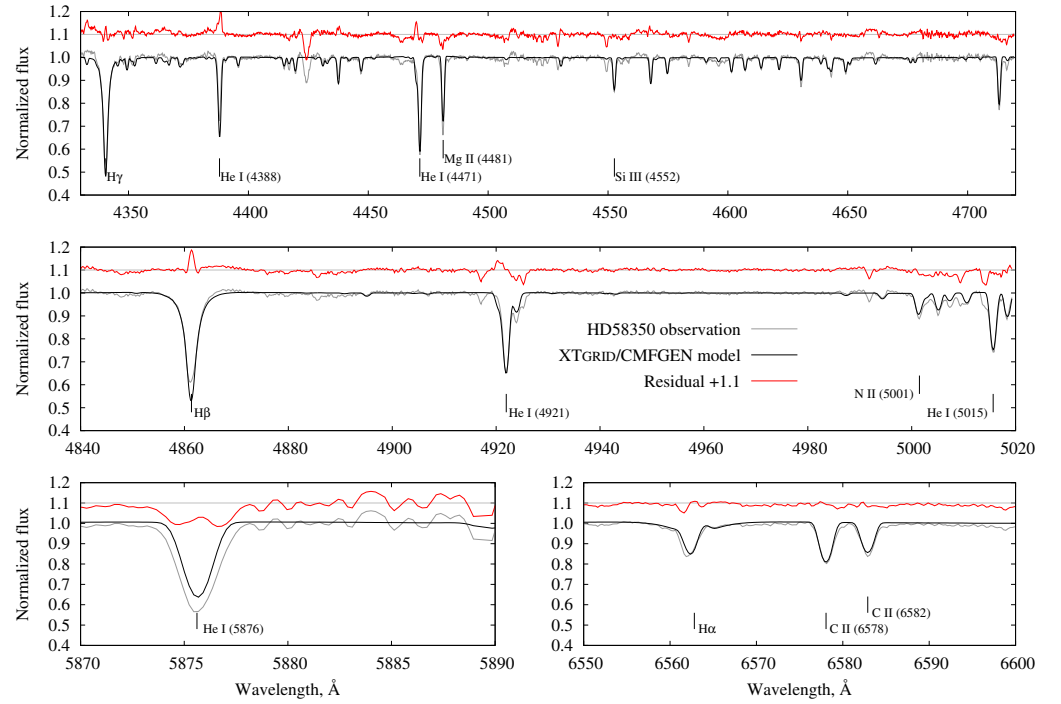


Figure 11. Best-fit XTGRID/CMFGEN model for HD 58350. In each panel, the CASLEO observation is in grey, the CMFGEN model in black, and the residuals, shifted by +1.1 for clarity, are in red.

Table 6. Summary of the spectroscopic results from unclumped CMFGEN models using the XTGRID fitting procedure. Abundances are reported on the 12 scale: $\epsilon = \log N_x/N_H + 12$. Fixed parameters are marked with an “x” prefix. Metals not listed here were included at their solar metallicity from [52].

Parameter	HD 42087		HD 52089		HD 58350	
T_{eff} (K)	$18,400^{+1000}_{-200}$		$23,800^{+3900}_{-1400}$		$15,800^{+100}_{-400}$	
$\log g$ (cms^{-2})	$2.34^{+0.01}_{-0.17}$		$3.40^{+0.01}_{-0.60}$		$1.95^{+0.02}_{-0.03}$	
$v \sin i$ (kms^{-1})	73.4 ± 8.0		38.4 ± 5.0		51.5 ± 5.0	
v_{turb} (kms^{-1})	x10		x10		x12	
\dot{M} ($M_{\odot} \text{ yr}^{-1}$)	$(2.3 \pm 1.0) \times 10^{-7}$		$(1.9 \pm 0.2) \times 10^{-8}$		$(6.2 \pm 2.0) \times 10^{-8}$	
v_{∞} (kms^{-1})	x700		x900		x230	
β	x2		x1		x3	
L_{\star} (L_{\odot})	$312,700^{+74000}_{-13000}$		$35,000^{+29200}_{-7500}$		$163,800^{+4200}_{-15900}$	
M_{\star} (M_{\odot})	24.3		11.1		9.5	
R_{\star} (R_{\odot})	x55		x11		x54	
$\log L_{\star}/M_{\star}$	4.1		3.5		4.2	
Mean atomic mass (a.m.u.)	1.4490		1.5097		1.5095	
Distance (pc)	2470^{+420}_{-290}		124 ± 2		608^{+148}_{-148}	
$E(B - V)$ (mag)	0.4		0.005		0.03	
Element	ϵ	mass fr.	ϵ	mass fr.	ϵ	mass fr.
Hydrogen	12	5.89×10^{-1}	12	5.52×10^{-1}	12	5.52×10^{-1}
Helium	$x11.23 \pm 0.10$	4.01×10^{-1}	$x11.30 \pm 0.17$	4.41×10^{-1}	$x11.31 \pm 0.12$	4.41×10^{-1}
Carbon	8.31 ± 0.08	1.37×10^{-3}	8.19 ± 0.15	1.04×10^{-3}	8.07 ± 0.08	7.75×10^{-4}
Nitrogen	8.12 ± 0.06	1.09×10^{-3}	7.97 ± 0.06	7.25×10^{-4}	8.21 ± 0.12	1.25×10^{-3}
Oxygen	8.60 ± 0.08	3.75×10^{-3}	8.30 ± 0.13	1.78×10^{-3}	8.19 ± 0.09	1.38×10^{-3}
Abundance ratios	[N/C]	[N/O]	[N/C]	[N/O]	[N/C]	[N/O]
	0.41	0.38	0.38	0.53	0.74	0.88

6. Discussion

We used the evolutionary sequences from Ekström et al. [22] to explore the evolutionary stage of our star sample. The main physical ingredients of these sequences relevant to our analysis include initial abundances of H, He, and metals set to $X = 0.720$, $Y = 0.266$, and $Z = 0.014$ with chemical initial abundances of $C = 2.283 \times 10^{-3}$, $N = 6.588 \times 10^{-4}$, and $O = 5.718 \times 10^{-3}$, in the mass fraction. We considered evolutionary tracks with differential rotation at two different rates: $\Omega/\Omega_{crit} = 0.568$ and $\Omega/\Omega_{crit} = 0.4$, employing for the latter an interpolation of the models with $\Omega/\Omega_{crit} = 0.568$ and 0, provided in Ekström et al. [22]. The mass-loss recipes employed in these sequences are those of Vink et al. [53] for initial masses above $7 M_{\odot}$. For initial masses above $15 M_{\odot}$ and $\log(T_{eff}) > 3.7$, de Jager et al. [54], the recipe was adopted and the correction factor for the radiative mass-loss rate from Maeder and Meynet [55] was implemented in these rotating models (see Equation (10) from Ekström et al. [22]). Detailed descriptions on the microphysics and mass-loss recipes employed in these evolutionary sequences can be found in Ekström et al. [22] and Yusof et al. [4]. Our selected stars with the derived T_{eff} , $\log L_{\star}$ and mass, along with the evolutionary tracks, are depicted in Figure 12. The errors in this Figure correspond to an error of 10% in the radii [11], which in turn result in a 21% error in the mass and luminosity.

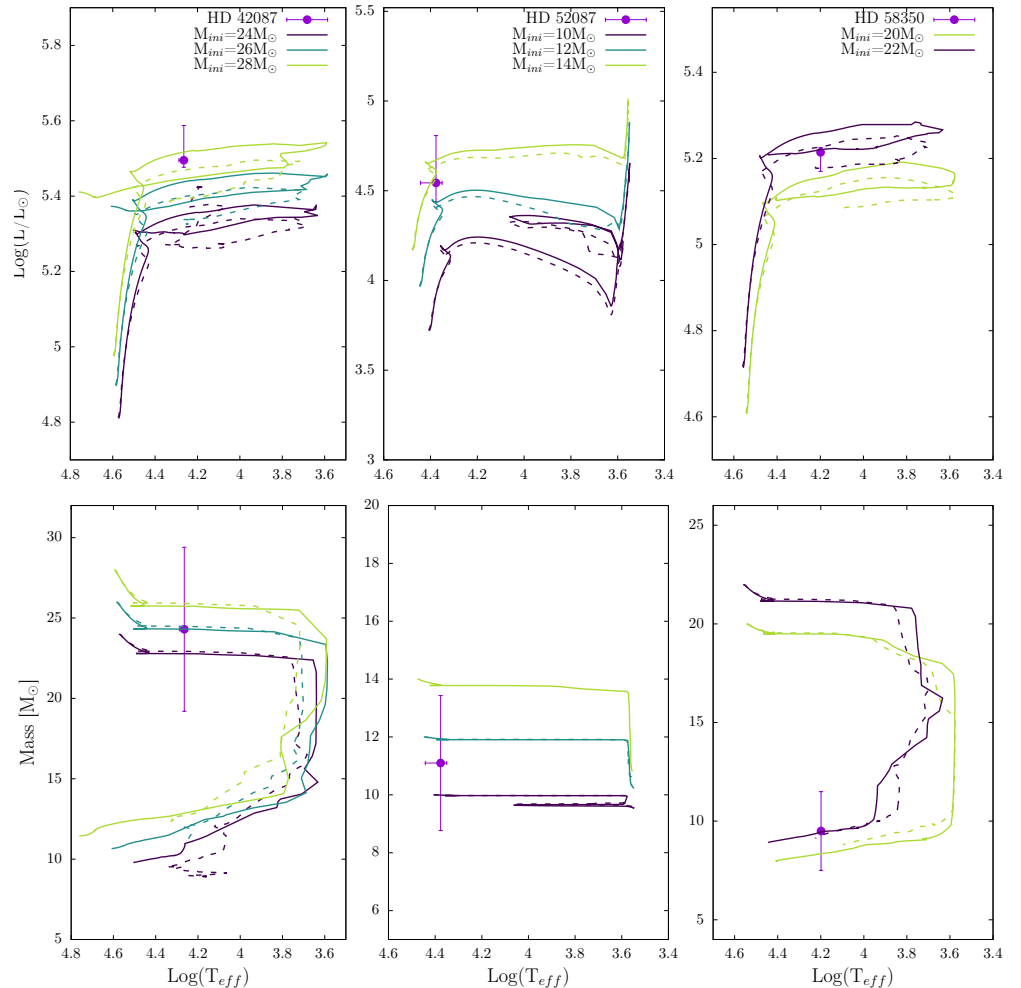


Figure 12. Left panels: HR diagram (**top**) and mass evolution (**bottom**) showing the position of HD 42087 and evolutionary tracks with initial masses of 24, 26, and 28 M_{\odot} . Middle panels: The same as in the left panels for HD 52087 and initial masses of 10, 12, and 14 M_{\odot} . Right panels: the same as before for HD 58350 and initial masses of 20 and 22 M_{\odot} . Solid and dashed lines represent models with $\Omega/\Omega_{crit} = 0.568$ from [22] and the interpolated ones for $\Omega/\Omega_{crit} = 0.4$, respectively.

Below, we discuss our results for each star in terms of their location in the HR diagram, their oscillations, and the mass-loss rate found; next, we compare our results on their surface abundances with previous studies.

6.1. HD 42087

In the left panel of Figure 12, we show the new position of HD 42087 in an HR diagram along with evolutionary tracks corresponding to initial masses of 24, 26, and 28 M_{\odot} . Continuous and dashed lines indicate rotation velocities of $\Omega/\Omega_{crit} = 0.568$ and $\Omega/\Omega_{crit} = 0.4$, respectively. In the lower panels, we include a diagram showing the total mass evolution. The derived values for T_{eff} and $\log(L_{*}/L_{\odot})$ suggest an initial mass of $\sim 26 M_{\odot}$; our value obtained for the current mass indicates that this star is at the pre-RSG stage, which is in agreement with the mass evolution diagram for stars with the mentioned initial mass.

Our analysis for this object resulted in a higher T_{eff} and lower $\log g$ than those from Searle et al. [17] and Haucke et al. [11]. We emphasize that Haucke et al. [11] did not have the Si lines covered by their spectra; in principle, our new values would be more reliable. Additionally, with our values, HD 42087 lies in the linear relation ($\log T_{eff} - \log g$) found in Searle et al. [17] for Galactic BSGs (their Figure 6). In Figure 13, we show the theoretical SED using the $D = 2470_{-289}^{+420}$ pc Gaia EDR3 distance and $E(B - V) = 0.4$ mag extinction adopted from the STILISM maps [56], along with the binned IUE spectrum in black. Our procedure uses the fit formula from Cardelli et al. [57] based on the extinction data from Fitzpatrick and Massa [58,59] with $R_v = 3.1$. The theoretical SED fits the photometric measurements, including the IUE spectrum, and the resulting SED and CMFGEN model masses agree within error bars, with 22.5 M_{\odot} being the mass derived from the SED. However, we were unable to match the $H\alpha$ and $H\beta$ profiles with our homogeneous wind models. Considering the reported line variability and asymmetries by Morel et al. [18], which is also obvious from Figure 2, we conclude that our steady and smooth wind model is inadequate for the 2020 CASLEO spectrum of HD 42087.

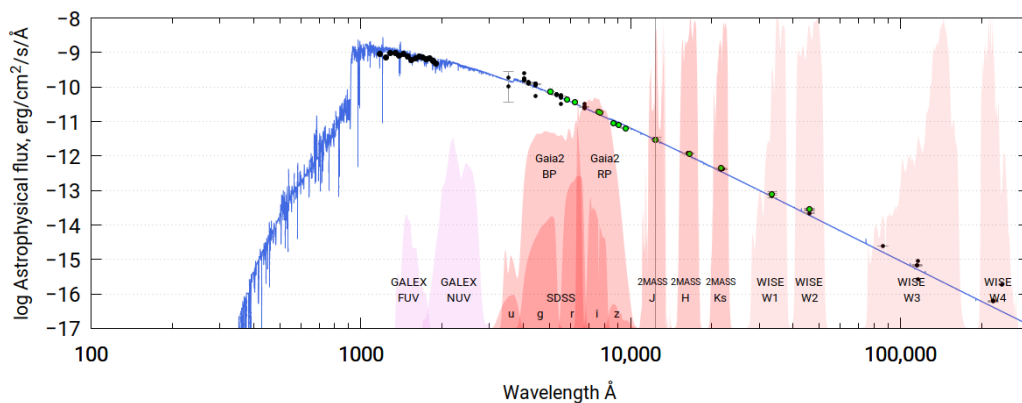


Figure 13. SED of HD 42087. All data points were taken from the VizieR Photometry Viewer service. The photometric data were de-reddened using $E(B - V) = 0.4$ mag. The green points were used to match the slope of the passband convolved CMFGEN fluxes to the observations, and the model was normalized to the observed SED in the 2MASS/J band. The binned IUE spectrum is included with black dots.

Nevertheless, we were able to derive a mass-loss rate of $\dot{M} = 2.3 \times 10^{-7} M_{\odot} \text{ yr}^{-1}$ for this star with our procedure. This value is close to the value found by Haucke et al. [11] of $\dot{M} = 5.7 \times 10^{-7} M_{\odot} \text{ yr}^{-1}$, being lower by a factor of ~ 2.6 . From looking at their observed $H\alpha$ line profile (taken in 2006, Figure 2), we see a stronger emission component in $H\alpha$ compared to our data (2020). This is in line with a higher mass-loss rate (in 2006) as found by these authors.

The frequency analysis performed for HD 42087 shows three frequencies, f_1 , f_2 , and f_3 , which appear randomly over the three sectors, with two more detectable in the long time span of the three consecutive sectors (f_4 and f_5). The short lifetime for these variations prevents us from associating them with stellar pulsations but rather with stochastic variations at the stellar surface [60]. Additionally, the analysis over the combined sectors allowed us to find one stable frequency, f_r , possibly associated with stellar pulsations. The nature of this mode is not certain. Its frequency lies in the usual range ([10, 100] d) of strange modes that are known to facilitate the mass loss in massive stars [12]. These modes can be radial and non-radial [61], and they appear trapped in the strongly inflated envelopes of highly non-adiabatic stars, usually with $\log L_*/M_* > 4$. The low amplitude of f_r and the new value found for $\log L_*/M_* = 4.1$ indicate that this can be a non-radial strange mode. If true, it would explain the high variability in the wind lines (Figure 2) and why the spectrum can not be modelled with a smooth wind approach. Nevertheless, the only way to determine whether this mode facilitates the mass loss in HD 42087 is to perform a nonlinear stability analysis and to check whether the mode velocity on the surface can exceed the stellar escape velocity. We did not detect any frequency corresponding to the ~ 25 d period observed for the variability in the H α line. We stress here that the detection of any periodicity from the H α profile in the light curves is unlikely to be observed. Any perturbation on the stellar surface produced in the large wind volume where the H α line is formed may lead to new perturbations (for example, due to densities and inhomogeneities in the wind), making its detection difficult. Furthermore, the H α profile, in most cases, is composed of absorption and emission components simultaneously, also hindering its detection. However, as shown in Krtićka and Feldmeier [60], wind variations can cause stochastic light variations if the base perturbations are sufficiently large. The lack of multiple independent frequencies identified as stellar pulsations modes in this object would indicate that this star belongs to the pre-RSG stage, considering that massive post-RSGs have in general more excited modes than pre-RSGs, as shown in Saio et al. [15]. This is in agreement with our values for T_{eff} , $\log g$, M_* (Figure 12).

6.2. HD 52089

The new position of HD 52089 in the HR diagram, along with evolutionary tracks for initial masses 10, 12, and 14 M_{\odot} and $\Omega/\Omega_{\text{crit}} = 0.568$ and 0.4 (continuous and dashed lines, respectively), are depicted in Figure 12. The HR diagram suggests initial masses between 12 and 14 M_{\odot} at the TAMS in agreement with our derived value for the current mass ($\sim 11M_{\odot}$) in this stage, considering the adopted errors in the mass. However, we cannot dismiss a merger scenario for this object that would explain the measured luminosity, which is slightly high considering an 11 M_{\odot} object at the TAMS. Such an event can lead to rejuvenation and an excess in the luminosity of the merger remnant due to the energy injection from the secondary star during the merging of the two components. The merger product might hence appear as if it would have a significantly higher mass. The best known such case is the B[e] supergiant star R4 in the Small Magellanic Cloud [62,63]. If true, then HD 52089 would be a highly important object to study merger remnants, and it would be interesting to search for possible remnants of ejecta from the past merger event.

Additionally, this star showed an inconsistency in the $T_{\text{eff}} - \log g$ distribution of [11], with a higher $\log g$ for its temperature than other stars in their sample. Our new fit to the 2015 CASLEO spectrum confirmed the earlier results and shows a discrepancy among the stellar mass, luminosity, and surface gravity, given its high effective temperature. With its close distance of $D = 124 \pm 2$ pc and moderate interstellar extinction of $E(B - V) = 0.005$ mag, adopted from [64] and STILISM, respectively, we find that its spectroscopic mass is in good agreement with the mass derived from the SED (9.8 M_{\odot}) depicted in Figure 14. We also notice the model from the optical fit matches the slope of the binned IUE spectrum, but there is an offset, possibly due to the low metallicity found for this object.

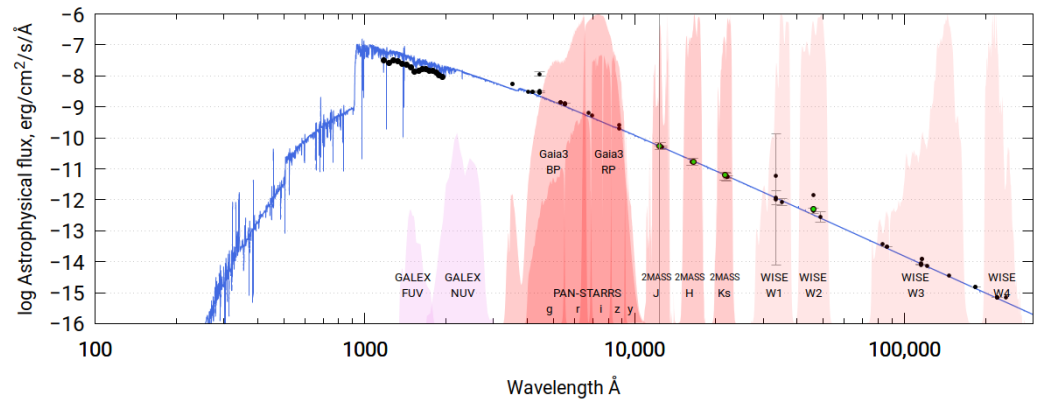


Figure 14. SED of HD 52089. Same as Figure 13, but de-reddening was conducted using $E(B - V) = 0.005$ mag.

The frequency analysis for HD 52089 over the 4 TESS sectors revealed one triplet centred in f_2 in Sector 33, corresponding to a rotational period of 5 d ($f_{rot} = 0.2 d^{-1}$). The short baseline observations provided by TESS single sectors translate into high Ray-light frequency separation, preventing making precise mode identification for short-term variabilities. In the case of f_3 , f_2 , and f_4 being members of a triplet, f_2 would be an $\ell = 1$ nonradial mode [15]. In this case, the star would have a surface rotation velocity of $\sim 110 \text{ km s}^{-1}$, considering the radius and rotation period derived for this object. Moreover, with the value of $v \sin i$ obtained from our analysis, we can derive the inclination of the star, which would be the ~ 20 degree. Besides the triplet, we found f_2 in Sectors 7 and 33, and signatures of this mode in Sectors 6 and 34 with very low amplitude (not included in Table 3) along with its harmonic supporting the hypothesis of f_2 being a non-radial mode due to its apparently extended lifetime. As in the case of HD 42087, we found low-frequency signals (f_1 , f_5 , and f_6) randomly excited over the observed sectors, which are probably related to convective variabilities stochastically excited at the stellar surface. These observations confirm the results of [65].

Our determination of \dot{M} for HD 52089, $\dot{M} = 1.9 \times 10^{-8} M_{\odot} \text{ yr}^{-1}$ agrees very well with the one reported by Haucke et al. [11]: $\dot{M} = 2.0 \times 10^{-8} M_{\odot}$. From comparing our observed H α line profile of this star, we do not find any significant morphological difference between the observed spectrum shown in Haucke et al. [11] and our data: a pure absorption H α line profile with flux at the core of the line of ~ 0.6 (normalized flux) (see Figure 3).

6.3. HD 58350

The right panel of Figure 12 shows the position of HD 58350 in the HR diagram and the evolution of the total mass along with evolutionary tracks for 20 and 22 M_{\odot} with different rotational velocities. We found an excellent agreement between our derived values for T_{eff} , $\log(L_{\star}/L_{\odot})$ and its current mass for a star evolution model with initial mass $\sim 22 M_{\odot}$ at the post-RSG stage, after losing a considerable amount of mass during its evolution. We notice as well that our derived values for the T_{eff} and $\log g$ are in good agreement with the linear relation found for galactic BSGs in Searle et al. [17].

The theoretical SED fits the optical photometric measurements for HD 58350 (Figure 15). We notice a slightly different slope for the IR photometric data, possibly pointing towards a time-variable wind in data taken at different dates. Considering its distance $D = 608 \pm 148 \text{ pc}$ [11], we derived an extinction $E(B - V) = 0.18 \text{ mag}$. We also found a discrepancy between the stellar masses obtained from the SED modeling ($\sim 5.5 M_{\odot}$) and the best-fitting CMFGEN model ($\sim 9.5 M_{\odot}$) of unclear origin. We have found different values for the effective temperature (and extinction) in the literature (see Section 2) for this object, ranging from 13,500 K to 16,000 K, possibly due to a combination between the use of different methodologies to derive it and due to stellar oscillations. This hampers a reliable comparison between our SED model and the photometric data, possibly leading to this

mass discrepancy. Spectroscopic time-series observations analyzed homogeneously can help to place reliable constraints on the effective temperature.

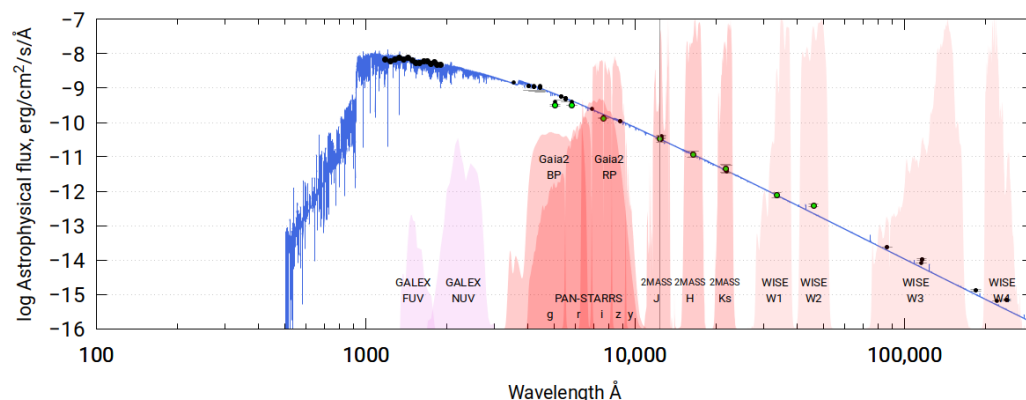


Figure 15. SED of HD 58350. Same as Figure 13, but de-reddening was conducted using $E(B - V) = 0.18$ mag (see main text).

For HD 58350, our derived \dot{M} of $6.2 \times 10^{-8} M_{\odot} \text{ yr}^{-1}$ is lower than the one from Haucke et al. [11] by a factor of ~ 2.4 . This can be understood since the observed $H\alpha$ line profile reported in Haucke et al. [11] (taken in 2006 and 2013) shows a more intense emission component in comparison with our data (very weak emission in $H\alpha$).

The frequency content for this star lies below $0.4 d^{-1}$. The only sector provided by TESS at the current time allowed us to find two independent frequencies. We were not able to find the frequency discovered in Lefever et al. [21], with $f = 0.1507 d^{-1}$, indicating that this mode is not an opacity-driven mode. From the analysis of one single TESS sector, we cannot suggest that this star is a non-radial oscillator. However, the marked $H\alpha$ line profile variation (see Figure 4) suggests that these frequencies are connected to line-driven wind instabilities [60]. The analysis in [15] demonstrated that a BSG in a post-RSG state should undergo multiple pulsations. It is therefore unfortunate that HD 58350, which is the best candidate in our sample for a post-RSG star, was observed only in one TESS sector. Only with multiple, and in particular consecutive TESS observations, would it be possible to properly analyze the frequency spectrum of this object and to confirm the theoretical predictions of Saio et al. [15].

6.4. Surface Abundances

With the aim of framing these discrepancies with our derived values for surface abundances, we compared our results with those from different authors and Geneva evolutionary tracks. Figure 16 shows our measured CNO abundances for the selected stars along with the solar abundances and the average CNO abundances derived in Searle et al. [17] for their Galactic BSG sample.

In general, for all three stars, we found well-constrained CNO abundances, all showing a slight depletion of C and O, and a mild overabundance of N when compared to the solar mixture. This pattern agrees with the previously reported CNO abundance profiles in Searle et al. [17]; however, at the same time, we found higher C and slightly lower O abundances. We notice that some systematic differences are expected from the analysis itself. The global spectral modeling applied in XTGRID is fundamentally different from the methodology of Searle et al. [17], who used different diagnostic lines for T_{eff} , $\log g$, and abundance determinations. Searle et al. [17] noted that their CMFGEN models, with derived C abundances from the C II 4267 Å line, overestimated the C II 6578 and 6582 Å lines. In contrast, our C abundance analysis was based on the strongest C features in the CASLEO observations (C II 6578 and 6582 Å lines), but the global analysis is also sensitive to variations in all other spectral lines due to a change in the C abundance. This difference in diagnostics is applied consistently for all surface and

wind parameters in the XTGRID. Furthermore, Nieva and Przybilla [66] showed that LTE analyses could result in discrepant abundances based on different carbon lines, and the C II 4267 multiplet tends to underestimate the carbon abundance. Further possible sources of a discrepancy may be the differences in atomic data used in the analyses and the different fit procedures. Additionally, we note that our sample of three stars is too small to match Searle et al. [17] population averages, and the individual objects in our selection may show large deviations. To uncover such systematics, one needs to process larger, homogeneously modeled datasets and multi-epoch observations, which are beyond the scope and limitations of our current work.

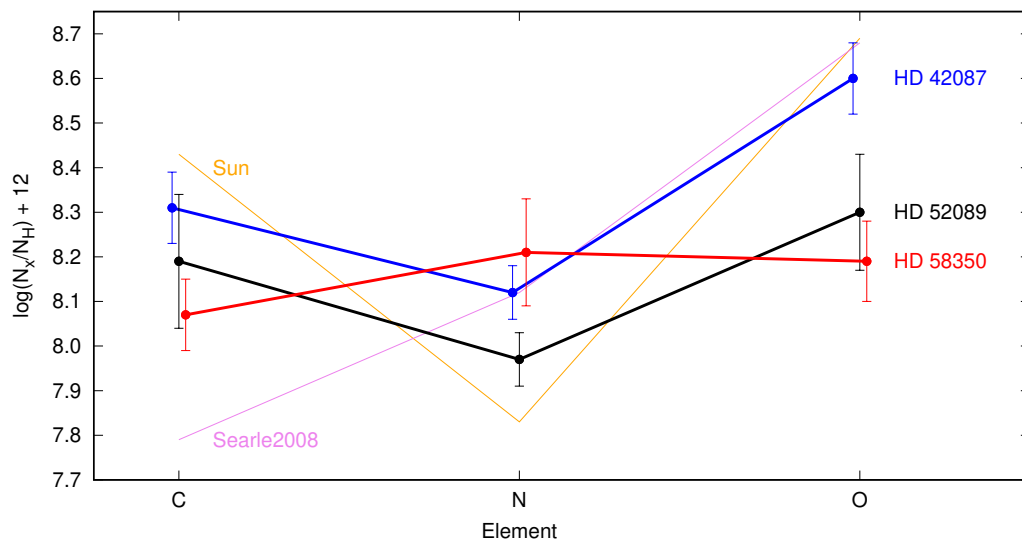


Figure 16. The measured CNO abundance patterns in all three stars compared to the solar pattern from Asplund et al. [52]. In all three stars, C and O are depleted and N is overabundant compared to the solar mixture. The mean CNO abundances found by Searle et al. [17] for Galactic BSGs are also shown for reference.

At the same time, we noticed that the total amount of metals we derived (see Table 6) correspond to subsolar metallicities, being approximately 70% Z_{\odot} , 60% Z_{\odot} , and 50% Z_{\odot} for HD 42087, HD 52089, and HD 58350, respectively, which is possibly due to the adopted fixed value for $n\text{He}/n\text{H} = 0.2$. We have also adopted fixed solar abundances for all metals beyond oxygen and did not include elements that do not contribute to the opacity, such as Ar, K, Ti, V, Mn, and Co. All these features contribute to reducing the metal mass fractions.

In Figure 17, we compare the N/C and N/O abundance ratios from different star samples with Geneva stellar evolution models for different masses. We included the sample of A and B supergiants studied in [17,67] and the B-type main sequence (MS) stars analyzed in [68] as a reference, along with our three stars. Three well-defined groups can be identified in the panels of Figure 17. B-type MS stars between 5 and 10 M_{\odot} form a clear sequence in temperature and show the lowest abundance ratios, which marks that these stars have low N abundances relative to C and O. Below $\sim 13,000$ K, cooler A-type supergiant stars show up as a compact group, while the hot side of the observed BSG abundance ratios shows a much larger scatter. The larger scatter can be interpreted in several ways. Kr̕tička et al. [69] have shown that winds are driven mostly by C, Si, and S for hot BSGs and iron for cooler BSGs, implying a decreasing mass-loss rate for temperatures lower than 15,000 K. A lower mass-loss rate might operate in favor of a better determination of N/C and N/O ratios. The observed compact group could also be a signature of the fast post-RSG evolution through the cool BSG stage. Additionally, atmospheres of cool supergiants usually exhibit more lines, helping to obtain precise values in their abundances. However, it is clear that none of the measurements reach the predicted high N/C and N/O ratios for the post-RSG domain.

Based on the abundance ratios alone, we find that all our stars are more consistent with a pre-RSG stage of evolution; we do not observe the predicted and very high N/C and N/O ratios. This is in contrast with the spectroscopic mass of HD 58350, which suggests that it is in a post-RSG stage. Saio et al. [15] showed that the N/C and N/O ratios are increased mainly by the mass loss. However, they found N/C and N/O abundances consistent with models at the pre-RSG stage, in contradiction with the position in the HR diagram for Deneb and Rigel, which arrive at the same conclusion.

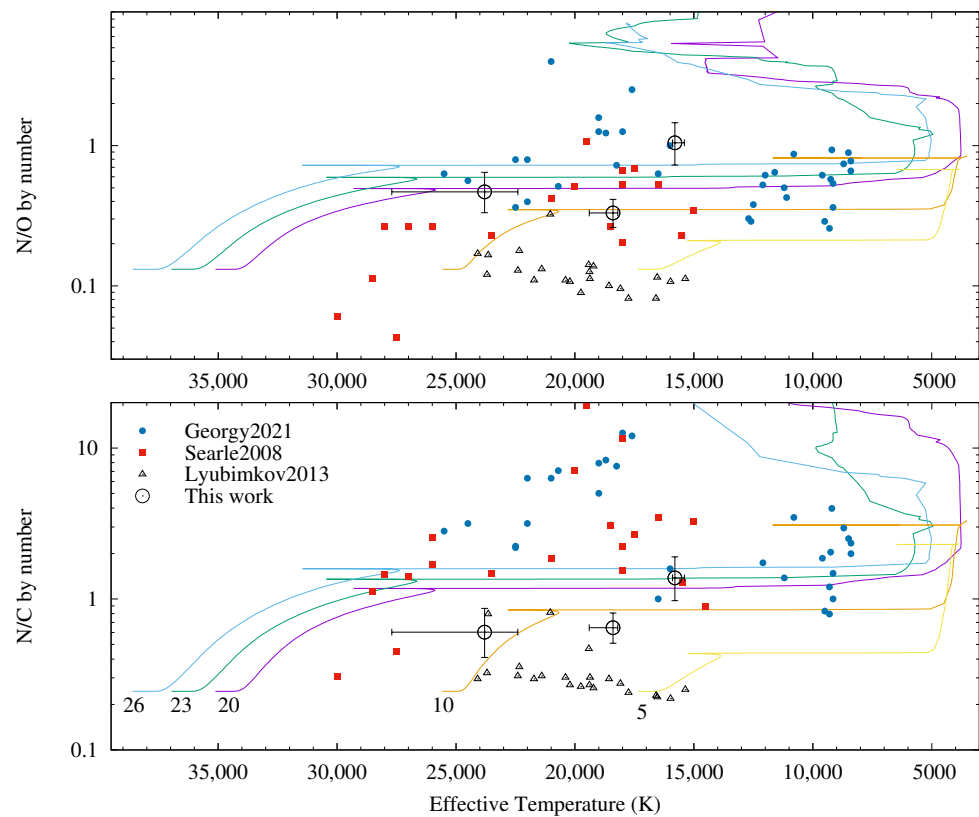


Figure 17. N/C (bottom) and N/O (top) abundance ratios by number from Searle et al. [17] and Georgy et al. [67] compared to our measurements, as well as Geneva solar metallicity ($Z = 0.014$), $\Omega/\Omega_{crit} = 0.4$ interpolated evolutionary tracks for 5, 10, 20, 23, and 26 M_{\odot} . For reference, we also show B-type main sequence stars from Lyubimkov et al. [68].

There is a discrepancy in the abundance ratios between evolutionary model predictions and spectroscopic measurements. The observed ratios remain significantly lower than predictions. Much larger samples, multifaceted efforts, and homogeneous modeling will be necessary to address this issue statistically.

Figure 18 shows the correlations between the N/O and N/C ratios, which is analogous to the distribution found for O-type stars in Martins et al. [70]. The offset between theoretical predictions and the measurements implies that some systematics may exist in the C and O abundances. A systematically underestimated C or overestimated O abundance can produce the observed offset. It is unlikely that all the methodologies used to analyze the surface abundances in these stars are biased in the same way; therefore, the origin of the offset remains unclear. It may be related to stellar variability as well as to atomic data or shortcomings in the surface abundance predictions. Martins et al. [70] demonstrated an anticorrelation between the N/C ratio and $\log g$; the lower the gravity, the larger the N/C ratio. Meanwhile, Saio et al. [15] concluded that recent developments in the modeling of RSG [71] make these stars more compact for a given luminosity. The combination of the two trends acts towards decreasing the offset with respect to the Geneva models in Figure 18.

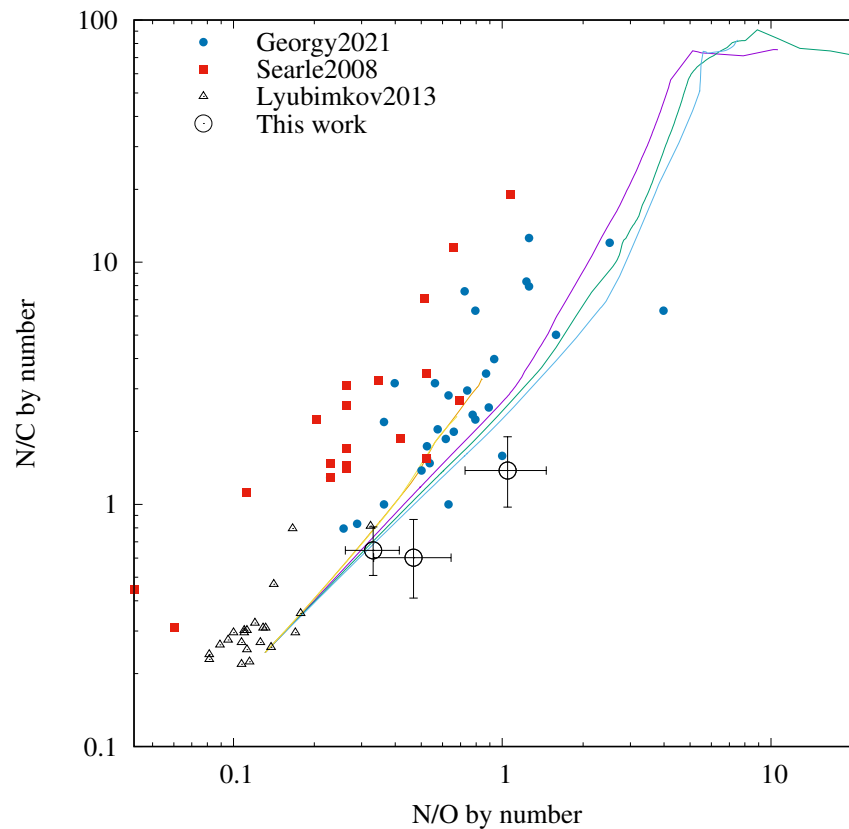


Figure 18. N/C and N/O abundance ratio correlations for our sample and the same tracks as in Figure 17. We included Searle et al. [17] and Geogy et al. [67] samples and the B-type main sequence stars from Lyubimkov et al. [68].

7. Conclusions

This paper reports our first step towards a comprehensive study of BSG stars, taking into account their photometric and spectroscopic variabilities.

The evolutionary tracks predict HD 42087 to be a pre-RSG star for our derived values of $\log(L_*/L_\odot)$, T_{eff} , and M_* , in agreement with our values for the abundance ratios. HD 52089 is most likely an $11 M_\odot$ star at the TAMS. However, we noticed that the derived luminosity is slightly high for an $11 M_\odot$ star, and a binary merger scenario is plausible. Finally, for HD 58350, the evolutionary tracks for our derived values indicate that this star is at the post-RSG. However, the derived surface abundance ratios are compatible with those at the pre-RSG stage, finding the same discrepancies mentioned in Saio et al. [15] for Deneb and Rigel. The rather short sectoral observing windows of TESS are insufficient to cover the low frequencies usually present in these stars. However, we were able to detect a frequency splitting allowing us to infer a rotational period of ~ 5 d for HD 52089 and to find a low frequency, $f_r = 0.093 \text{ d}^{-1}$, related possibly to strange mode instabilities in HD 42089 in agreement with its new derived value for the $\log(L_*/M_*)$.

We found lower values for mass-loss rates of HD 42097 and HD 58350 compared with those derived by Haucke et al. [11], in agreement with the detected variability of the $H\alpha$ emission component, related to changes in the wind mass-loss rate in these stars at these different epochs. The finding of low-frequencies stochastic oscillations in these objects is possibly connected with such variations.

Despite the numerous and valuable efforts to study BSG stars, there are still many issues to address; here, we highlight the most important ones:

- A large sample of BSGs needs to be studied with homogeneously modeled datasets of multi-epoch observations, with the aim of uncovering systematic deviations of surface abundance ratios from evolutionary models. Additionally, multi-epoch observations

will allow us to place constraints on the current uncertainties observed in the radii of these objects and to identify changes in radii caused by radial pulsations.

- To frame the current studies for the needed M_{core}/M_r ratio for massive stars to evolve back towards the blue region of the HR diagram, such as the effect of stellar rotation, convective boundaries criteria, mixing length theories, overshooting that is adopted for the stellar interior, and evolutionary models, in terms of the CNO abundances. This will allow us to untackle the observed indetermination in the evolutionary stage of these objects with precise values for their CNO surface abundances and, in turn, will help to set the needed constraints to the current poorly established theoretical mass-loss recipes in the diverse evolutionary states and mass ranges.
- In addition, we emphasize that stellar pulsations play a key role in the analysis of BSGs, not only as a test to infer their evolutionary stage, as proposed in Saio et al. [15], but also as a mechanism that facilitates the mass loss in massive stars, as suggested in Kraus et al. [10] and theoretically confirmed in Yadav and Glatzel [72], affecting, therefore, their surface abundances. The systematic differences noticed when comparing evolutionary tracks with surface abundance measurements for BSGs (Figure 18) should be discussed, considering the effect of stellar pulsations over their evolution. Furthermore, short-term mass-loss variabilities should be contemplated in detailed evolutionary sequences, as they can act as an additional source for the discrepancies found with evolutionary models.

From a spectral analysis software development point, we have added CMFGEN modeling capabilities to the automatic spectral analysis procedure XTGRID². The first results shown here demonstrate its feasibility for processing spectra of massive stars and deriving homogeneous parameters from diverse data. The next steps will include improving the accuracy of spectral inference to reduce the observed discrepancies in mass and surface abundances. Additionally, we will work on better optimizing the calculations by recycling previously calculated models. Future applicability for large datasets relies on the development of efficient methods to search the parameter space, either by utilizing large grids [73] and/or machine learning techniques.

We would like to mention, as well, that we found diffuse interstellar bands (DIB) in the spectra of HD 42087 and HD 58350. The 4428 and 6613 Å DIB bands are clearly present in both stars. Neither of the two bands is visible in the spectrum of the relatively nearby HD 52089. Although the two stars with DIBs are at larger distances, and they have very different extinction values, the DIBs show very similar strengths. The lack of DIBs in HD 52089 is likely due to its short distance and the very low interstellar extinction in its direction. In addition, HD 52089 is not only the hottest star in our sample, but also the strongest ultraviolet source in the night sky [74], which may be able to photodissociate DIB carriers.

Author Contributions: Conceptualization, J.P.S.A., P.N. and M.K.; methodology, J.P.S.A., P.N. and E.S.d.G.d.A.; software, P.N.; validation, P.N. and E.S.d.G.d.A.; formal analysis, P.N.; investigation, J.P.S.A., P.N., E.S.d.G.d.A., M.K. and M.A.R.D.; resources, M.A.R.D. and M.H.; writing—original draft preparation, J.P.S.A., P.N., M.A.R.D., M.K. and E.S.d.G.d.A.; writing—review and editing, J.P.S.A., P.N., E.S.d.G.d.A. and M.K.; visualization, J.P.S.A., P.N., M.K. and M.A.R.D.; supervision, J.P.S.A.; project administration, J.P.S.A. and P.N. All authors have read and agreed to the published version of the manuscript.

Funding: This research received funding from the European Union’s Framework Programme for Research and Innovation Horizon 2020 (2014–2020) under the Marie Skłodowska-Curie Grant Agreement №823734 (POEMS project). The Astronomical Institute in Ondřejov is supported by the project RVO:67985815. J.P.S.A. and M.K. acknowledge financial support from the Czech Science foundation (GAČR 20-00150S). E.S.G.A. has been financially supported by ANID Fondecyt postdoctoral grant folio № 3220776. P. N. acknowledges support from the Grant Agency of the Czech Republic (GAČR 22-34467S). M.A.R.D. acknowledges support from CONICET (PIP 1337).

Data Availability Statement: The data underlying this article will be shared on reasonable request to the corresponding author.

Acknowledgments: We are grateful to the referees for their thoughtful reports and useful suggestions that helped us improve the manuscript. Based on observations taken with the J. Saade Telescope at Complejo Astronómico El Leoncito (CASLEO), operated under an agreement between the Consejo Nacional de Investigaciones Científicas y Técnicas de la República Argentina, the Secretaría de Ciencia y Tecnología de la Nación, and the National Universities of La Plata, Córdoba, and San Juan. This research has used the services of www.Astroserver.org under reference M1DE05 (accessed on 20 August 2023).

Conflicts of Interest: The authors declare no conflict of interest. The funders had no role in the design of the study; in the collection, analyses, or interpretation of data; in the writing of the manuscript; or in the decision to publish the results’.

Notes

- ¹ IRAF is distributed by the National Optical Astronomy Observatory, which is operated by the Association of Universities for Research in Astronomy (AURA) under a cooperative agreement with the National Science Foundation.
- ² <https://xtgrid.astroserver.org/>, (accessed on 20 August 2023).

References

1. Abbott, D.C. The return of mass and energy to the interstellar medium by winds from early-type stars. *Astrophys. J.* **1982**, *263*, 723–735. [[CrossRef](#)]
2. Martins, F.; Palacios, A. A comparison of evolutionary tracks for single Galactic massive stars. *Astron. Astrophys.* **2013**, *560*, A16. [[CrossRef](#)]
3. Agrawal, P.; Szécsi, D.; Stevenson, S.; Eldridge, J.J.; Hurley, J. Explaining the differences in massive star models from various simulations. *Mon. Not. RAS* **2022**, *512*, 5717–5725. [[CrossRef](#)]
4. Yusof, N.; Hirschi, R.; Eggenberger, P.; Ekström, S.; Georgy, C.; Sibony, Y.; Crowther, P.A.; Meynet, G.; Kassim, H.A.; Harun, W.A.W.; et al. Grids of stellar models with rotation VII: Models from 0.8 to 300 M_{\odot} at supersolar metallicity ($Z = 0.020$). *Mon. Not. RAS* **2022**, *511*, 2814–2828. [[CrossRef](#)]
5. Maeder, A.; Meynet, G. Evolution of massive stars with mass loss and rotation. *New Astron. Rev.* **2010**, *54*, 32–38. [[CrossRef](#)]
6. Wagle, G.A.; Ray, A.; Dev, A.; Raghu, A. Type IIP Supernova Progenitors and Their Explodability. I. Convective Overshoot, Blue Loops, and Surface Composition. *Astrophys. J.* **2019**, *886*, 27. [[CrossRef](#)]
7. Bowman, D.M.; Bursens, S.; Pedersen, M.G.; Johnston, C.; Aerts, C.; Buysschaert, B.; Michielsen, M.; Tkachenko, A.; Rogers, T.M.; Edelmann, P.V.F.; et al. Low-frequency gravity waves in blue supergiants revealed by high-precision space photometry. *Nat. Astron.* **2019**, *3*, 760–765. [[CrossRef](#)]
8. Langer, N. Presupernova Evolution of Massive Single and Binary Stars. *Annu. Rev. Astron. Astrophys.* **2012**, *50*, 107–164. [[CrossRef](#)]
9. Glatzel, W. On the origin of strange modes and the mechanism of related instabilities. *Mon. Not. RAS* **1994**, *271*, 66. [[CrossRef](#)]
10. Kraus, M.; Haucke, M.; Cidale, L.S.; Venero, R.O.J.; Nickeler, D.H.; Németh, P.; Niemczura, E.; Tomić, S.; Aret, A.; Kubát, J.; et al. Interplay between pulsations and mass loss in the blue supergiant 55 Cygnus = HD 198 478. *Astron. Astrophys.* **2015**, *581*, A75. [[CrossRef](#)]
11. Haucke, M.; Cidale, L.S.; Venero, R.O.J.; Curé, M.; Kraus, M.; Kanaan, S.; Arcos, C. Wind properties of variable B supergiants. Evidence of pulsations connected with mass-loss episodes. *Astron. Astrophys.* **2018**, *614*, A91. [[CrossRef](#)]
12. Aerts, C.; Lefever, K.; Baglin, A.; Degroote, P.; Oreiro, R.; Vučković, M.; Smolders, K.; Acke, B.; Verhoelst, T.; Desmet, M.; et al. Periodic mass-loss episodes due to an oscillation mode with variable amplitude in the hot supergiant HD 50064. *Astron. Astrophys.* **2010**, *513*, L11. [[CrossRef](#)]
13. Saio, H.; Kuschnig, R.; Gautschy, A.; Cameron, C.; Walker, G.A.H.; Matthews, J.M.; Guenther, D.B.; Moffat, A.F.J.; Rucinski, S.M.; Sasselov, D.; et al. MOST Detects g- and p-Modes in the B Supergiant HD 163899 (B2 Ib/II). *Astrophys. J.* **2006**, *650*, 1111–1118. [[CrossRef](#)]
14. Ostrowski, J.; Daszyńska-Daszkiewicz, J. Pulsations in B-type supergiants with masses $M < 20 M_{\odot}$ before and after core helium ignition. *Mon. Not. RAS* **2015**, *447*, 2378–2386. [[CrossRef](#)]
15. Saio, H.; Georgy, C.; Meynet, G. Evolution of blue supergiants and α Cygni variables: Puzzling CNO surface abundances. *Mon. Not. RAS* **2013**, *433*, 1246–1257. [[CrossRef](#)]
16. Németh, P.; Kawka, A.; Vennes, S. A selection of hot subluminescent stars in the GALEX survey - II. Subdwarf atmospheric parameters. *Mon. Not. RAS* **2012**, *427*, 2180–2211. [[CrossRef](#)]
17. Searle, S.C.; Prinja, R.K.; Massa, D.; Ryans, R. Quantitative studies of the optical and UV spectra of Galactic early B supergiants. I. Fundamental parameters. *Astron. Astrophys.* **2008**, *481*, 777–797. [[CrossRef](#)]
18. Morel, T.; Marchenko, S.V.; Pati, A.K.; Kuppaswamy, K.; Carini, M.T.; Wood, E.; Zimmerman, R. Large-scale wind structures in OB supergiants: A search for rotationally modulated $H\alpha$ variability. *Mon. Not. RAS* **2004**, *351*, 552–568. [[CrossRef](#)]

19. Morel, T.; Hubrig, S.; Briquet, M. Nitrogen enrichment, boron depletion and magnetic fields in slowly-rotating B-type dwarfs. *Astron. Astrophys.* **2008**, *481*, 453–463. [[CrossRef](#)]
20. Fossati, L.; Castro, N.; Morel, T.; Langer, N.; Briquet, M.; Carroll, T.A.; Hubrig, S.; Nieva, M.F.; Oskinova, L.M.; Przybilla, N.; et al. B fields in OB stars (BOB): On the detection of weak magnetic fields in the two early B-type stars β CMa and ϵ CMa. Possible lack of a “magnetic desert” in massive stars. *Astron. Astrophys.* **2015**, *574*, A20. [[CrossRef](#)]
21. Lefever, K.; Puls, J.; Aerts, C. Statistical properties of a sample of periodically variable B-type supergiants. Evidence for opacity-driven gravity-mode oscillations. *Astron. Astrophys.* **2007**, *463*, 1093–1109. [[CrossRef](#)]
22. Ekström, S.; Georgy, C.; Eggenberger, P.; Meynet, G.; Mowlavi, N.; Wyttenbach, A.; Granada, A.; Decressin, T.; Hirschi, R.; Frischknecht, U.; et al. Grids of stellar models with rotation. I. Models from 0.8 to 120 M_{\odot} at solar metallicity ($Z = 0.014$). *Astron. Astrophys.* **2012**, *537*, A146. [[CrossRef](#)]
23. Ricker, G.R.; Winn, J.N.; Vanderspek, R.; Latham, D.W.; Bakos, G.Á.; Bean, J.L.; Berta-Thompson, Z.K.; Brown, T.M.; Buchhave, L.; Butler, N.R.; et al. Transiting Exoplanet Survey Satellite (TESS). In *Space Telescopes and Instrumentation 2014: Optical, Infrared, and Millimeter Wave*; Oschmann, J.M., Clampin, M., Fazio, G.G., MacEwen, H.A., Eds.; Society of Photo-Optical Instrumentation Engineers (SPIE) Conference Series; SPIE: Bellingham, WA, USA, 2014; Volume 9143, p. 914320. [[CrossRef](#)]
24. Ricker, G.R.; Winn, J.N.; Vanderspek, R.; Latham, D.W.; Bakos, G.Á.; Bean, J.L.; Berta-Thompson, Z.K.; Brown, T.M.; Buchhave, L.; Butler, N.R.; et al. Transiting Exoplanet Survey Satellite (TESS). *J. Astron. Telesc. Instruments Syst.* **2015**, *1*, 014003. [[CrossRef](#)]
25. Ginsburg, A.; Sipőcz, B.M.; Brasseur, C.E.; Cowperthwaite, P.S.; Craig, M.W.; Deil, C.; Guillochon, J.; Guzman, G.; Liedtke, S.; Lian Lim, P.; et al. astroquery: An Astronomical Web-querying Package in Python. *Astron. J.* **2019**, *157*, 98. [[CrossRef](#)]
26. Lightkurve Collaboration; Cardoso, J.V.d.M.; Hedges, C.; Gully-Santiago, M.; Saunders, N.; Cody, A.M.; Barclay, T.; Hall, O.; Sagar, S.; Turtelboom, E.; et al. *Lightkurve: Kepler and TESS Time Series Analysis in Python*; Astrophysics Source Code Library: College Park, MD, USA, 2018. Available online: <https://arxiv.org/pdf/2111.14278.pdf> (accessed on 16 March 2023).
27. Garcia, S.; Van Reeth, T.; De Ridder, J.; Tkachenko, A.; Ijspeert, L.; Aerts, C. Detection of period-spacing patterns due to the gravity modes of rotating dwarfs in the TESS southern continuous viewing zone. *Astron. Astrophys.* **2022**, *662*, A82. [[CrossRef](#)]
28. Lenz, P.; Breger, M. Period04 User Guide. *Commun. Asteroseismol.* **2005**, *146*, 53–136. [[CrossRef](#)]
29. Baran, A.S.; Koen, C. A Detection Threshold in the Amplitude Spectra Calculated from TESS Time-Series Data. *Acta Astron.* **2021**, *71*, 113–121. [[CrossRef](#)]
30. Hillier, D.J.; Miller, D.L. The Treatment of Non-LTE Line Blanketing in Spherically Expanding Outflows. *Astrophys. J.* **1998**, *496*, 407–427. [[CrossRef](#)]
31. Bouret, J.C.; Hillier, D.J.; Lanz, T.; Fullerton, A.W. Properties of Galactic early-type O-supergiants. A combined FUV-UV and optical analysis. *Astron. Astrophys.* **2012**, *544*, A67. [[CrossRef](#)]
32. de Almeida, E.S.G.; Hugbart, M.; Domiciano de Souza, A.; Rivet, J.P.; Vakili, F.; Siciak, A.; Labeyrie, G.; Garde, O.; Matthews, N.; Lai, O.; et al. Combined spectroscopy and intensity interferometry to determine the distances of the blue supergiants P Cygni and Rigel. *Mon. Not. RAS* **2022**, *515*, 1–12. [[CrossRef](#)]
33. Bouret, J.C.; Lanz, T.; Martins, F.; Marcolino, W.L.F.; Hillier, D.J.; Depagne, E.; Hubeny, I. Massive stars at low metallicity. Evolution and surface abundances of O dwarfs in the SMC. *Astron. Astrophys.* **2013**, *555*, A1. [[CrossRef](#)]
34. Hillier, D.J.; Davidson, K.; Ishibashi, K.; Gull, T. On the Nature of the Central Source in η Carinae. *Astrophys. J.* **2001**, *553*, 837–860. [[CrossRef](#)]
35. Eversberg, T.; Lépine, S.; Moffat, A.F.J. Outmoving Clumps in the Wind of the Hot O Supergiant ζ Puppis. *Astrophys. J.* **1998**, *494*, 799–805. [[CrossRef](#)]
36. Bouret, J.C.; Lanz, T.; Hillier, D.J. Lower mass loss rates in O-type stars: Spectral signatures of dense clumps in the wind of two Galactic O4 stars. *Astron. Astrophys.* **2005**, *438*, 301–316. [[CrossRef](#)]
37. Martins, F.; Marcolino, W.; Hillier, D.J.; Donati, J.F.; Bouret, J.C. Radial dependence of line profile variability in seven O9-B0.5 stars. *Astron. Astrophys.* **2015**, *574*, A142. [[CrossRef](#)]
38. Sander, A.A.C. Recent advances in non-LTE stellar atmosphere models. In *Proceedings of the The Lives and Death-Throes of Massive Stars*; Eldridge, J.J.; Bray, J.C.; McClelland, L.A.S.; Xiao, L., Eds., 2017; Volume 329, pp. 215–222. Available online: <https://www.cambridge.org/core/journals/proceedings-of-the-international-astronomical-union/article/recent-advances-in-nonlte-stellar-atmosphere-models/B993A4F409FCE7BACF9DAE43CCCF908B> (accessed on 16 March 2023). [[CrossRef](#)]
39. Martins, F.; Schaerer, D.; Hillier, D.J.; Meynadier, F.; Heydari-Malayeri, M.; Walborn, N.R. On stars with weak winds: The Galactic case. *Astron. Astrophys.* **2005**, *441*, 735–762. [[CrossRef](#)]
40. Marcolino, W.L.F.; Bouret, J.C.; Martins, F.; Hillier, D.J.; Lanz, T.; Escolano, C. Analysis of Galactic late-type O dwarfs: More constraints on the weak wind problem. *Astron. Astrophys.* **2009**, *498*, 837–852. [[CrossRef](#)]
41. de Almeida, E.S.G.; Marcolino, W.L.F.; Bouret, J.C.; Pereira, C.B. Probing the weak wind phenomenon in Galactic O-type giants. *Astron. Astrophys.* **2019**, *628*, A36. [[CrossRef](#)]
42. Rivet, J.P.; Siciak, A.; de Almeida, E.S.G.; Vakili, F.; Domiciano de Souza, A.; Fouché, M.; Lai, O.; Vernet, D.; Kaiser, R.; Guerin, W. Intensity interferometry of P Cygni in the H α emission line: Towards distance calibration of LBV supergiant stars. *Mon. Not. RAS* **2020**, *494*, 218–227. [[CrossRef](#)]
43. Hubeny, I.; Lanz, T. Non-LTE Line-blanketed Model Atmospheres of Hot Stars. I. Hybrid Complete Linearization/Accelerated Lambda Iteration Method. *Astrophys. J.* **1995**, *439*, 875. [[CrossRef](#)]

44. Lanz, T.; Hubeny, I. A Grid of NLTE Line-blanketed Model Atmospheres of Early B-Type Stars. *Astrophys. J. Suppl.* **2007**, *169*, 83–104. [[CrossRef](#)]
45. Hubeny, I.; Lanz, T. TLUSTY User's Guide III: Operational Manual. *arXiv* **2017**, arXiv:1706.01937. <https://doi.org/10.48550/arXiv.1706.01937>.
46. Lin, J.; Wu, C.; Wang, X.; Németh, P.; Xiong, H.; Wu, T.; Filippenko, A.V.; Cai, Y.; Brink, T.G.; Yan, S.; et al. An 18.9 min blue large-amplitude pulsator crossing the 'Hertzsprung gap' of hot subdwarfs. *Nat. Astron.* **2023**, *7*, 223–233. [[CrossRef](#)]
47. Lei, Z.; He, R.; Németh, P.; Zou, X.; Xiao, H.; Yang, Y.; Zhao, J. Mass distribution for single-lined hot subdwarf stars in LAMOST. *arXiv* **2023**, arXiv:2306.15342. <https://doi.org/10.48550/arXiv.2306.15342>.
48. Németh, P.; Vos, J.; Molina, F.; Bastian, A. The first heavy-metal hot subdwarf composite binary SB 744. *Astron. Astrophys.* **2021**, *653*, A3. [[CrossRef](#)]
49. Luo, Y.; Németh, P.; Li, Q. Hot Subdwarf Stars Identified in Gaia DR2 with Spectra of LAMOST DR6 and DR7. II. Kinematics. *Astrophys. J.* **2020**, *898*, 64. [[CrossRef](#)]
50. Wang, K.; Németh, P.; Luo, Y.; Chen, X.; Jiang, Q.; Cao, X. Extremely Low-mass White Dwarf Stars Observed in Gaia DR2 and LAMOST DR8. *Astrophys. J.* **2022**, *936*, 5. [[CrossRef](#)]
51. Vennes, S.; Németh, P.; Kawka, A.; Thorstensen, J.R.; Khalack, V.; Ferrario, L.; Alper, E.H. An unusual white dwarf star may be a surviving remnant of a subluminous Type Ia supernova. *Science* **2017**, *357*, 680–683. [[CrossRef](#)]
52. Asplund, M.; Grevesse, N.; Sauval, A.J.; Scott, P. The Chemical Composition of the Sun. *Annu. Rev. Astron Astrophys.* **2009**, *47*, 481–522. [[CrossRef](#)]
53. Vink, J.S.; de Koter, A.; Lamers, H.J.G.L.M. Mass-loss predictions for O and B stars as a function of metallicity. *Astron. Astrophys.* **2001**, *369*, 574–588. [[CrossRef](#)]
54. de Jager, C.; Nieuwenhuijzen, H.; van der Hucht, K.A. Mass loss rates in the Hertzsprung-Russell diagram. *Astron. Astrophys. Suppl.* **1988**, *72*, 259–289.
55. Maeder, A.; Meynet, G. Stellar evolution with rotation. VI. The Eddington and Omega -limits, the rotational mass loss for OB and LBV stars. *Astron. Astrophys.* **2000**, *361*, 159–166. [[CrossRef](#)]
56. Capitanio, L.; Lallement, R.; Vergely, J.L.; Elyajouri, M.; Monreal-Ibero, A. Three-dimensional mapping of the local interstellar medium with composite data. *Astron. Astrophys.* **2017**, *606*, A65. [[CrossRef](#)]
57. Cardelli, J.A.; Clayton, G.C.; Mathis, J.S. The Relationship between Infrared, Optical, and Ultraviolet Extinction. *Astrophys. J.* **1989**, *345*, 245. [[CrossRef](#)]
58. Fitzpatrick, E.L.; Massa, D. An Analysis of the Shapes of Ultraviolet Extinction Curves. I. The 2175 Angstrom Bump. *Astrophys. J.* **1986**, *307*, 286. [[CrossRef](#)]
59. Fitzpatrick, E.L.; Massa, D. An Analysis of the Shapes of Ultraviolet Extinction Curves. II. The Far-UV Extinction. *Astrophys. J.* **1988**, *328*, 734. [[CrossRef](#)]
60. Krtićka, J.; Feldmeier, A. Stochastic light variations in hot stars from wind instability: finding photometric signatures and testing against the TESS data. *Astron. Astrophys.* **2021**, *648*, A79. [[CrossRef](#)]
61. Saio, H. Linear analyses for the stability of radial and non-radial oscillations of massive stars. *Mon. Not. RAS* **2011**, *412*, 1814–1822. [[CrossRef](#)]
62. Zickgraf, F.J.; Kovacs, J.; Wolf, B.; Stahl, O.; Kaufer, A.; Appenzeller, I. R4 in the Small Magellanic Cloud: A spectroscopic binary with a B[e]/LBV-type component. *Astron. Astrophys.* **1996**, *309*, 505–514.
63. Wu, S.; Everson, R.W.; Schneider, F.R.N.; Podsiadlowski, P.; Ramirez-Ruiz, E. The Art of Modeling Stellar Mergers and the Case of the B[e] Supergiant R4 in the Small Magellanic Cloud. *Astrophys. J.* **2020**, *901*, 44. [[CrossRef](#)]
64. van Leeuwen, F. Validation of the new Hipparcos reduction. *Astron. Astrophys.* **2007**, *474*, 653–664. [[CrossRef](#)]
65. Burssens, S.; Simón-Díaz, S.; Bowman, D.M.; Holgado, G.; Michielsen, M.; de Burgos, A.; Castro, N.; Barbá, R.H.; Aerts, C. Variability of OB stars from TESS southern Sectors 1-13 and high-resolution IACOB and OWN spectroscopy. *Astron. Astrophys.* **2020**, *639*, A81. [[CrossRef](#)]
66. Nieva, M.F.; Przybilla, N. C II Abundances in Early-Type Stars: Solution to a Notorious Non-LTE Problem. *Astrophys. J. Lett.* **2006**, *639*, L39–L42. [[CrossRef](#)]
67. Georgy, C.; Saio, H.; Meynet, G. Blue supergiants as tests for stellar physics. *Astron. Astrophys.* **2021**, *650*, A128. [[CrossRef](#)]
68. Lyubimkov, L.S.; Lambert, D.L.; Poklad, D.B.; Rachkovskaya, T.M.; Rostopchin, S.I. Carbon, nitrogen and oxygen abundances in atmospheres of the 5–11 M_⊙ B-type main-sequence stars. *Mon. Not. RAS* **2013**, *428*, 3497–3508. [[CrossRef](#)]
69. Krtićka, J.; Kubát, J.; Krtićková, I. New mass-loss rates of B supergiants from global wind models. *Astron. Astrophys.* **2021**, *647*, A28. [[CrossRef](#)]
70. Martins, F.; Hervé, A.; Bouret, J.C.; Marcolino, W.; Wade, G.A.; Neiner, C.; Alecian, E.; Grunhut, J.; Petit, V. The MiMeS survey of magnetism in massive stars: CNO surface abundances of Galactic O stars. *Astron. Astrophys.* **2015**, *575*, A34. [[CrossRef](#)]
71. Davies, B.; Kudritzki, R.P.; Plez, B.; Trager, S.; Lançon, A.; Gazak, Z.; Bergemann, M.; Evans, C.; Chiavassa, A. The Temperatures of Red Supergiants. *Astrophys. J.* **2013**, *767*, 3. [[CrossRef](#)]
72. Yadav, A.P.; Glatzel, W. Stability analysis, non-linear pulsations and mass loss of models for 55 Cygni (HD 198478). *Mon. Not. RAS* **2016**, *457*, 4330–4339. [[CrossRef](#)]

73. Zsargó, J.; Fierro-Santillán, C.R.; Klapp, J.; Arrieta, A.; Arias, L.; Valencia, J.M.; Sigalotti, L.D.G.; Hareter, M.; Puebla, R.E. Creating and using large grids of precalculated model atmospheres for a rapid analysis of stellar spectra. *Astron. Astrophys.* **2020**, *643*, A88. [[CrossRef](#)]
74. Gregorio, A.; Stalio, R.; Broadfoot, L.; Castelli, F.; Hack, M.; Holberg, J. UVSTAR observations of Adara (epsilon CMa): 575-1250 Å. *Astron. Astrophys.* **2002**, *383*, 881–891. [[CrossRef](#)]

Disclaimer/Publisher's Note: The statements, opinions and data contained in all publications are solely those of the individual author(s) and contributor(s) and not of MDPI and/or the editor(s). MDPI and/or the editor(s) disclaim responsibility for any injury to people or property resulting from any ideas, methods, instructions or products referred to in the content.